Canadian
Journal of Physics

A NUCLEAR MAGNETIC RESONANCE STUDY OF COLEMANITE[1]

F. HOLUJ[2] AND H. E. PETCH

ABSTRACT

A single crystal of colemanite, $CaB_3O_4(OH)_3.H_2O$, which is known to be ferro-electric at temperatures below about $-2°$ C, has been investigated by means of nuclear magnetic resonance (n.m.r.) techniques. The B^{11} resonances are split because the nuclear Zeeman levels are perturbed by the interactions between the nuclear electric quadrupole moments and the electric field gradients existing at the boron sites. The splittings have been examined in detail at room temperature and at $-40°$ C. The results have been analyzed and the quadrupole coupling constants, the asymmetry parameters, and the orientations of the principal axes of the electric field gradient tensors existing at the boron sites at room tempera-ture and $-40°$ C are reported. Selected B^{11} resonance lines have been examined over the temperature range $40°$ C to $-120°$ C with particular emphasis on the region about $0°$ C where a phase transition occurs. The complex proton signal was also studied over the same temperature range. Abrupt broadening of this signal occurred at the phase transition. These studies revealed that the crystal may transform from its centrosymmetrical room-temperature (point group $2/m$) form either to a metastable monoclinic form with point group 2 or to a triclinic form with point group 1. It is not clear whether two transitions, separated by only about $3°$ C, are involved or whether there is only one transition with two alternative arrangements, differing only slightly in activation energy, available to the structure. The transition or transitions are of the second-order displacive type. Where possible, the results have been interpreted in terms of the crystal structure.

INTRODUCTION

The mineral colemanite, $CaB_3O_4(OH)_3.H_2O$, has aroused keen interest because it was the first boron-containing material known to be ferroelectric. On the basis of their X-ray investigations of colemanite at room temperature, Christ, Clark, and Evans (1958) proposed a centrosymmetrical structure which is consistent with the space group $P2_1/a$. However, Davisson (1956) observed that colemanite is weakly piezoelectric and pyroelectric at room temperature and concluded that colemanite lacks a center of symmetry. At the same time Davisson found indications that colemanite undergoes a phase transition; the pyroelectric constant shows an exceedingly high and narrow peak at $-2.5°$ C and an anomaly exists in the dielectric constant at this temperature. Goldsmith

(1956) found, in agreement with the work of Davisson, a sharp dielectric anomaly centered at $-2.5°$ C and also discovered that colemanite is ferroelectric below this temperature. However, the dielectric breakdown patterns (Davisson 1956) remain centrosymmetrical over a wide range of temperatures including that of the transition. Furthermore, there is no optical evidence of a phase change and, at the time this work was undertaken, there was no X-ray evidence either.

The object of this investigation was threefold: (1) to obtain quantitative data on the B^{11} quadrupole coupling tensors in the room temperature and ferroelectric phases of colemanite, (2) to resolve the discrepancies regarding the symmetry of colemanite, and (3) to detect, if possible, the phase transition and study its progress as a function of temperature.

THEORY

A nucleus of spin I and magnetic moment $\boldsymbol{\mu}$ placed in a magnetic field $\mathbf{H_0}$ has available to it $2I+1$ equally spaced Zeeman levels. The $2I$ transitions between adjacent levels give rise to a single absorption line at the Larmor frequency $\nu_0 = \mu H_0/hI$. If the nucleus also possesses an electric quadrupole moment eQ and is situated in an electric field with a non-vanishing gradient $\nabla \mathbf{E}$ then, as Pound (1950) has shown, each of the Zeeman levels is perturbed, and the single line is split into $2I$ components.

We have studied experimentally this so-called quadrupolar splitting of the B^{11} $(I = 3/2)$ resonance in colemanite and have analyzed our data following the method developed by Volkoff (1953) for the case where the electric quadrupole interaction is weak compared with the interaction between the nuclear magnetic dipoles and $\mathbf{H_0}$. For convenience of reference and to establish notation, a summary of the relevant theory, specialized to the case $I = 3/2$, is reproduced below. Each unique nuclear site gives rise to three lines: a central line ν_c from the transition $m = +1/2 \rightleftarrows -1/2$, and two "satellites" ν_{s_1} and ν_{s_2} from the transitions $m = \pm 3/2 \rightleftarrows \pm 1/2$. According to standard perturbation theory, the frequencies of the central line and of the centroid of the satellites, $1/2(\nu_{s_1}+\nu_{s_2})$, show no displacement from ν_0 provided the quadrupole interaction is so weak that it is permissible to neglect all perturbation terms higher than the first. The frequency difference between the two satellites is given, for a rotation of the crystal about any axis maintained perpendicular to $\mathbf{H_0}$, by

$$(1) \qquad \nu_{s_2} - \nu_{s_1} = a + b \cos 2\theta + c \sin 2\theta$$

where θ is the angle of rotation. In the case of somewhat stronger quadrupole coupling, the first-order perturbation term may be inadequate and the second-order perturbation term must also be used. The second-order term contributes nothing new to the splitting of the satellites, but predicts a shift from ν_0 of the centroid of the satellites and of the central line. Thus, for a rotation about any axis perpendicular to $\mathbf{H_0}$

$$(2) \qquad \bar{\nu} - \nu_0 = \bar{n} + \bar{p} \cos 2\theta + \bar{r} \sin 2\theta + \bar{u} \cos 4\theta + \bar{v} \sin 4\theta$$

$$(3) \qquad \nu_c - \nu_0 = n + p \cos 2\theta + r \sin 2\theta + u \cos 4\theta + v \sin 4\theta$$

where $\bar{\nu}$ stands for $1/2(\nu_{s_1}+\nu_{s_2})$, the centroid of the pair of satellites. Note that equation (1) neglects perturbation terms of third and higher odd order while equations (2) and (3) neglect perturbation terms of fourth and higher even order.

If the crystal is rotated in turn about each of three mutually perpendicular axes X, Y, Z which are fixed with respect to the crystal, then three independent sets of the coefficients a, b, c, n, p, r, u, v may be obtained from the experimentally observed curves of the dependence of $\nu_{s_2}-\nu_{s_1}$, $\bar{\nu}-\nu_0$, and $\nu_c-\nu_0$ on θ_X, θ_Y, and θ_Z (the subscripts denote the rotation axes). These coefficients are related to the components of the quadrupole coupling tensor $\psi_{ij} = eQ\phi_{ij}/h$ (where ϕ is the electrostatic potential at the nuclear site and $\phi_{ij} \equiv \partial^2\phi/\partial q_i\partial q_j$) expressed in terms of the X, Y, Z axes. For the X rotation, the coefficients in equation (1) are given by

$$\begin{aligned} a_X &= 1/2(\psi_{YY}+\psi_{ZZ}), \\ b_X &= 1/2(\psi_{YY}-\psi_{ZZ}), \\ c_X &= -\psi_{YZ}. \end{aligned}$$

(4)

Corresponding relations for the rotations about the Y and Z axes may be obtained by a cyclic permutation of the subscripts. As a consequence of Laplace's equation

(5)
$$\begin{aligned} a_X &= 1/2(b_Y-a_Y) = -1/2(b_Z+a_Z), \\ b_X &= -1/2(3a_Y+b_Y) = 1/2(3a_Z-b_Z). \end{aligned}$$

These identities are useful as a check on the experimental accuracy.

The coefficients in equation (2) for the shift of the centroid of the pair of satellites in the X rotation are related to the coefficients in equation (1) by

(6)
$$\begin{aligned} \bar{n}_X &= (b_X^2+c_X^2+c_Y^2+c_Z^2)/12\nu_0, \\ \bar{p}_X &= -(c_Y^2-c_Z^2)/12\nu_0, \\ \bar{r}_X &= -c_Y c_Z/6\nu_0, \\ \bar{u}_X &= -(b_X^2-c_X^2)/12\nu_0, \\ \bar{v}_X &= -b_X c_X/6\nu_0. \end{aligned}$$

Also, in equation (3) for the shift of the central line $\nu_c-\nu_0$ in the X rotation, the coefficients can be written as

(7)
$$\begin{aligned} n_X &= [18a_X^2-7(b_X^2+c_X^2)-4(c_Y^2+c_Z^2)]/96\nu_0, \\ p_X &= [-a_X b_X+c_Y^2-c_Z^2]/8\nu_0, \\ r_X &= [-a_X c_X+2c_Y c_Z]/8\nu_0, \\ u_X &= 3(b_X^2-c_X^2)/32\nu_0, \\ v_X &= 3b_X c_X/16\nu_0. \end{aligned}$$

Again, corresponding relations for the rotations about the Y and Z axes may be obtained by a cyclic permutation of the subscripts.

The experimental values of n, p, r, u, v lead to values of a, b, c. These, combined with the values of a, b, c, obtained directly from the $\nu_{s_2}-\nu_{s_1}$ data,

lead, through equations (4), to values for the components of the quadrupole coupling tensor ψ_{ij} in the X, Y, Z co-ordinate system. The relative, but not the absolute, signs of these components are determined because in this experiment it was not possible to find out which of the two observed satellites ν_{s_1}, ν_{s_2} corresponded to which of the two transitions $m = \pm 3/2 \rightleftharpoons \pm 1/2$.

This tensor can then be diagonalized by standard procedures to yield the quadrupole coupling constant, $C_z \equiv eQ\phi_{zz}/h$, and the asymmetry parameter, $\eta \equiv (\phi_{xx} - \phi_{yy})/\phi_{zz}$. The process of diagonalization will also give, with respect to the X, Y, Z axes, the direction cosines of the principal axes x, y, z of the electric field gradient tensor. For a second rank tensor the orientation but not the sense of the principal axes is significant so only the relative signs of the direction cosines are determined.

So far we have considered only the interactions of the nuclei with $\mathbf{H}_0$ and with $\nabla \mathbf{E}$. In a later section, dealing with the proton resonance spectrum, we shall be concerned with a magnetic dipole–dipole interaction between nuclei. From a classical point of view this may be regarded in the following manner. Each nucleus finds itself not only in the externally applied magnetic field $\mathbf{H}_0$, but also in a small local field $\mathbf{H}_{loc}$ produced by neighboring nuclear dipoles. The direction of $\mathbf{H}_{loc}$ varies from one nuclear site to another, depending on the positions and relative orientations of the other nuclear dipoles in the lattice. Since the field produced by a magnetic dipole decreases as $1/r^3$, $\mathbf{H}_{loc}$ at a nuclear site is determined mainly by the nearest neighbors. It follows that the total magnetic field will vary by a few gauss from one nuclear site to another. As a consequence, the resonance condition is not sharp and the signal will be broadened. If the interacting nuclei are identical, spin-exchange processes will limit the lifetime of a given spin state. The resultant uncertainty in the energy of the state will cause a further broadening of the resonance signal.

In cases where the nuclei each interact strongly with several neighbors, the calculation of the shape of the resonance signal is too complex for an exact solution except for arrangements of high symmetry. Fortunately, Van Vleck (1948) has developed a quantitative relationship between the nuclear configuration and the so-called second moment of the line shape. This quantity, the average value of the square of the frequency deviation from the center of the resonance, is defined as

$$(8) \qquad \langle (\Delta\nu)^2 \rangle_{av} \equiv \int_{-\infty}^{\infty} (\nu - \nu_0)^2 g(\nu) d\nu$$

where $g(\nu)$ is a normalized function taken to represent the shape of the absorption line plotted versus frequency. The result of VanVleck's theorem shows that the second moment can be expressed as

$$(9) \qquad \langle (\Delta\nu)^2 \rangle_{av} = (3/2) I(I+1)(g^4 \mu_0^4/\hbar^2) N^{-1} \sum (3\cos^2\theta_{jk}-1)^2 r_{jk}^{-6}$$
$$+ (1/3)(g^2 \mu_0^4/\hbar^2) N^{-1} \sum_{j,f} I_f(I_f+1) g_f^2 (3\cos^2\theta_{jf}-1)^2 r_{jf}^{-6}$$

where μ_0 is the nuclear magneton; g, I are the nuclear g-factor and spin for the resonant nuclei, respectively; g_f, I_f are the nuclear g-factors and spins,

respectively, for other nuclides in the sample; r_{st} is the distance between nuclei s and t; θ_{st} is the angle between $\mathbf{H}_0$ and the vector from nucleus s to t; and N is the number of nuclei within the volume to which the broadening interactions are considered to be confined in calculating $\langle(\Delta\nu)^2\rangle_{av}$.

Equation (9) was developed for a rigid array of nuclei. In the event that the atoms or molecules containing the interacting nuclei may have vibrational, rotational, or translational motion, the resonance line shape and its second moment may be profoundly altered. If the orientation rate is much greater than the resonance line-width, the function $(3\cos^2\theta_{jk}-1)$ must be averaged over the motion resulting in a decreased line-width and second moment.

One can now predict the expected behavior of the width of a resonance line as the temperature is varied. At very low temperatures the signal from the solid material will be very broad (of the order several tens of kilocycles per second) and will remain fairly constant in width as the temperature is increased until at a transition from an effectively rigid system to a rapidly reorienting system the signal is abruptly narrowed.

THE COLEMANITE CRYSTAL

Colemanite, $CaB_3O_4(OH)_3 \cdot H_2O$, is a mineral found in California, U.S.A., usually in conjunction with other boron-containing minerals. The crystals are generally small, colorless, transparent, prismatic, and elongated along [001]. The crystallographic data as obtained by Christ (1953) are summarized below:

monoclinic; space group: $P2_1/a$, C_{2h}^5;

$a = 8.743\pm0.004$ Å, $b = 11.264\pm0.002$ Å, $c = 6.102\pm0.003$ Å;

$\beta = 110°\ 7'\pm5'$;

cell contents: $4[CaB_3O_4(OH)_3 \cdot H_2O]$.

Christ, Clark, and Evans (1958), using X-ray techniques, have established the structure of colemanite. It contains infinite boron–oxygen chains running parallel to the a axis, linked together laterally by ionic bonds through Ca^{2+} ions to form sheets parallel to (010). The sheets, in turn, are linked together through a system of hydrogen bonds involving the hydroxyl groups of the chains and the water molecules. The chain element has the composition $[B_3O_4(OH)_3]^{2-}$ and consists of a BO_3 triangle, a $BO_3(OH)$ tetrahedron, and a $BO_2(OH)_2$ tetrahedron linked at corners to form a ring. The structure is shown in projection on (001) in Fig. 1.

In many ferroelectric materials, hydrogen atoms play a dominant role in the ferroelectric behavior; accordingly, we shall pay particular attention to the positions of the hydrogen atoms in the colemanite structure proposed by Christ *et al.* The calcium, boron, and oxygen atoms show up prominently on the electron density projections. However, it was necessary for Christ *et al.* to infer the positions of the hydrogen atoms from the configuration of these heavier atoms. As shown in Fig. 1, only one oxygen atom (O_8) in the asymmetric unit is not bonded to a boron atom; this atom must therefore be identified as part of the water molecule. Neighboring water molecules are separated by 2.73 Å and, following the arguments of Christ *et al.*, are joined by a hydrogen bond. Since there is a center of symmetry lying midway between
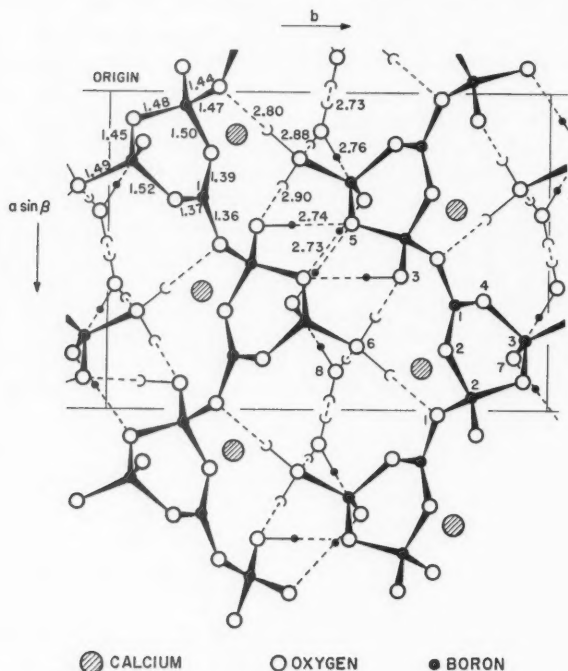
FIG. 1.   A projection of the structure of colemanite on (001). The dashed lines indicate the postulated hydrogen bonds. The smallest circles indicate the probable positions of the hydrogen atoms, with a whole circle designating a site occupied full time by a hydrogen atom, and a half-circle designating a site occupied half time by a hydrogen atom. Information taken from Christ *et al.* (1958).

the two water molecules, it must be assumed that the hydrogen atom in the bond is contributed half the time by one molecule and half the time by the other. The water molecule lies at distances of 2.76 and 2.88 Å from O_7 and O_6, respectively. This suggests that a normal hydrogen bond links the water molecule and O_7 and that the water molecule, when it is not contributing a hydrogen atom to the water–water bond, is directing a hydrogen bond toward O_6. The remaining three hydrogen atoms must be associated in hydroxyl groups with O_3, O_6, and O_7 since the remaining four oxygens are linked to two boron atoms each. The hydroxyl groups O_3 and O_7 appear to be linked by hydrogen bonds to O_5, since the oxygen–oxygen distances are 2.74 Å and 2.73 Å, respectively. The hydroxyl group O_6 lies 2.80 Å from the oxygen atom O_1 and 2.90 Å from the oxygen atom in the hydroxyl group O_3. This suggests that it directs a hydrogen bond toward these two atoms, each about half the time. In this way, Christ *et al.* have assigned all the hydrogen atoms to full-time hydrogen bonds of average length 2.74 Å and

half-time hydrogen bonds of average length 2.87 Å. The existence of "half-time" bonds implies a disordered state, which, of course, may be either dynamic or static. The X-ray data cannot distinguish.

Christ *et al.* believe that the key to the ferroelectric behavior of colemanite lies in the hydrogen bonds. They suggest that the disorder in the hydrogen bonds is dynamic and that, at the transition temperature, the hydrogen bonds between the water molecules become permanently polarized in an ordered arrangement to give rise to a spontaneous polarization. The hydroxyl O_6 may also become permanently bonded, below the transition point, to either O_1 or O_3.

APPARATUS AND EXPERIMENTAL PROCEDURE

The nuclear magnetic resonance spectrometer, of conventional design, consisted of an oscillating detector of the type described by Volkoff, Petch, and Smellie (1952), a narrow-band audio amplifier tuned to the magnetic field modulation frequency (210 c.p.s.), a Schuster-type phase-sensitive detector (1951), and a recording milliammeter. The externally applied magnetic field, produced by a 12-in. Varian electromagnet, was monitored by means of a proton resonance signal displayed on an oscilloscope. A General Radio heterodyne frequency meter Type 620-A, with the aid of a Hallicrafter Model SX-62A communications receiver, was used to make frequency measurements with an accuracy of about 0.5 kc/sec.

The original crystal mount and dial assembly, which were used for the measurements obtained at room temperature, permitted the axis, about which the crystal was rotated, to be made perpendicular to the magnetic field to within about 20 minutes of arc and the rotation angle θ to be read to within 0.3°. For work at temperatures other than room temperature, an improved crystal mount and dial assembly were constructed. The use of a larger dial and a circular vernier made it possible to read the rotation angle to 0.1° and the arc system from an X-ray goniometer incorporated into the crystal mount made it possible to orient the rotation axis so that it was perpendicular to the magnetic field to within 5 minutes of arc. In this apparatus, the crystal mount, crystal, and coil assembly were all located inside an insulated, virtually airtight cell which was provided with an inlet and outlet. The temperature of the crystal was controlled by a blast of air which was circulated through a system of heat exchangers in series with the cell. It was possible to maintain the temperature of the crystal, as measured by a thermocouple, to within 0.5° C of any desired temperature in the range −120° C to +50° C.

A number of crystals and cleavage fragments of colemanite from Inyo and San Bernardino counties, California, U.S.A., were used in our preliminary n.m.r. studies. The individual lines in the B^{11} n.m.r. spectra of most of these samples were found to be very broad. Ordinarily this would not have been too serious, but in the case of colemanite the spectrum is complex with a large number of lines (a maximum of 29 can be resolved at low temperatures) and the separations between many of the lines are unusually small so that

the excessive breadth of the signals made it impossible to resolve them over large ranges of crystal orientation. Also, some lines were apparently so broadened at certain crystal orientations that it was not possible to detect them. Presumably this excessive broadening was due to impurities or internal stresses in the crystals.

For all the work reported here, a transparent cleavage fragment of colemanite from San Bernardino county, which gave much narrower lines, was used. This sample was roughly L-shaped and approximately 2 cm $\times$ 1 cm $\times$ 1.5 cm in size. It possessed two perfect (010) cleavages, one perfect and one striated (110) face, and a distinct, but imperfect, cleavage parallel to (001). The intersection, along a 2-cm edge, of a perfect (010) cleavage plane and the perfect (110) face defined the c axis. The crystal orientation was deduced from morphological features and confirmed by X-ray diffraction. The X, Y, and Z axes were chosen parallel to the $\mathbf{b} \times \mathbf{c}$, $\mathbf{b}$, and $\mathbf{c}$ directions, respectively, because the external features of the crystal made it easy to recognize these directions. The rotation angles θ_X, θ_Y, and θ_Z were measured between $\mathbf{H}_0$ and the Y, Z, and X axes respectively.

For a given rotation, the crystal was first mounted as accurately as possible on the basis of its external features with the desired axis parallel to the rotation axis and then very accurately oriented by observing the "crossovers" in the B^{11} spectra. For each of the three rotations, the B^{11} n.m.r. spectra were recorded at 15° intervals from 0° to 360°. Where these data were insufficient to establish the rotation patterns unambiguously, additional spectra were taken at intermediate orientations. At a few orientations certain lines were so close together that they could not be resolved. In such cases, the frequencies were interpolated from additional readings taken at orientations where the lines could be resolved.

EXPERIMENTAL RESULTS

1. The B^{11} Spectrum of Colemanite at Room Temperature

(a) Qualitative Analysis of the Spectrum

The spin of B^{11} is known to be 3/2 so that a "simple" spectrum of only three lines, a central component ν_c and two satellites ν_{s_1} and ν_{s_2}, would be expected if all the boron sites in a crystal were equivalent. Actually the B^{11} spectrum in colemanite is considerably more complex, consisting of a maximum of 15 resolved lines as is shown in Fig. 2A. The frequencies of the lines depend strongly upon the angular orientation of the crystal except for that of the very intense line denoted ν_0 which remains constant at the calculated unperturbed value. Whenever the crystal orientation is such that the b crystallographic axis is either parallel or perpendicular to the magnetic field direction, a number of the lines coincide to produce a "reduced" spectrum, Fig. 2B, of seven lines in addition to the strong central line, ν_0. The line widths, as defined by the two maxima in the derivative of each absorption line, were of the order of 5 kc/sec but they did vary to some extent depending upon the orientation of the crystal. The relative intensities did not vary appreciably with changes in the crystal orientation.
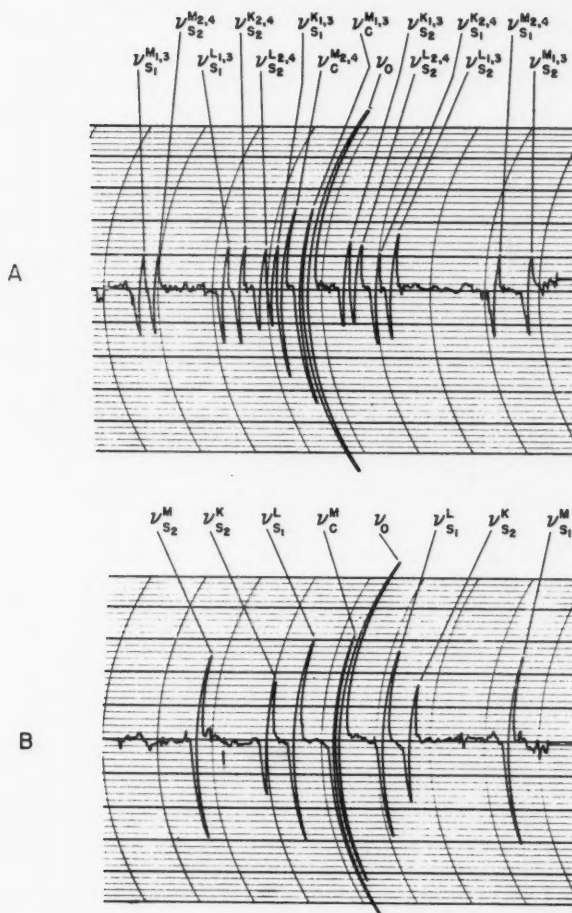
FIG. 2. Selected recordings of the derivatives of the B^{11} absorption lines in colemanite at room temperature. The nomenclature of the lines is explained in the text. The frequency scale is approximately 107 kc/sec per chart division.

(A) This recording shows the maximum number of resolved lines. It was obtained with a crystal orientation such that the Y axis made an angle of 135° with H_0 and the X and Z axes made angles of 10° and 80°, respectively, with the normal to the plane containing H_0 and the Y axis.

(B) An example of the reduced spectrum obtained at the crystal orientation $\theta_Y = 150°$.

The frequency variations of the lines are plotted in Figs. 3, 4, and 5 for the three rotations about X, Y, and Z. Note that for the complete Y rotation the spectrum is reduced since the b axis is maintained perpendicular to H_0. Each pair of rotations has one orientation in common (e.g., $\theta_X = 0°$ and $\theta_Z = 90°$ both correspond with the b axis parallel to H_0) so lines arising

FIG. 3. The dependence on angular position of the B^{11} resonance lines in colemanite at room temperature for the X rotation.

from a given nuclear site can be identified in the various rotations. A detailed inspection of Figs. 3, 4, and 5 reveals that the lines can be classified on the basis of their angular dependence. The eight lines denoted $\nu_{s_1}^{K1,3}$, $\nu_{s_2}^{K1,3}$, $\nu_{s_1}^{K2,4}$, $\nu_{s_2}^{K2,4}$, $\nu_{s_1}^{L1,3}$, $\nu_{s_2}^{L1,3}$, $\nu_{s_1}^{L2,4}$, and $\nu_{s_2}^{L2,4}$ are never separated from the frequency of the line denoted ν_0 by more than about 150 kc/sec and they occur in pairs with the two members of each pair symmetrically situated on opposite sides of the

FIG. 4. The dependence on angular position of the B^{11} resonance lines in colemanite at room temperature for the Y rotation.

line ν_0, i.e., $\bar{\nu}$ coincides with ν_0. They are obviously satellite lines arising from four non-identical sets of sites at which the quadrupole interaction is weak. The frequencies of the central lines arising from these four sites should be almost exactly equal to the unperturbed frequency and independent of the crystal orientation because the energy difference between nuclear $m = +1/2$ and $m = -1/2$ states is virtually unchanged when the quadrupole interaction is weak. The line ν_0 is much more intense than any other line and, as the crystal orientation is changed, its frequency remains constant at the calculated unperturbed value. Hence it is reasonable to consider ν_0 to consist of the
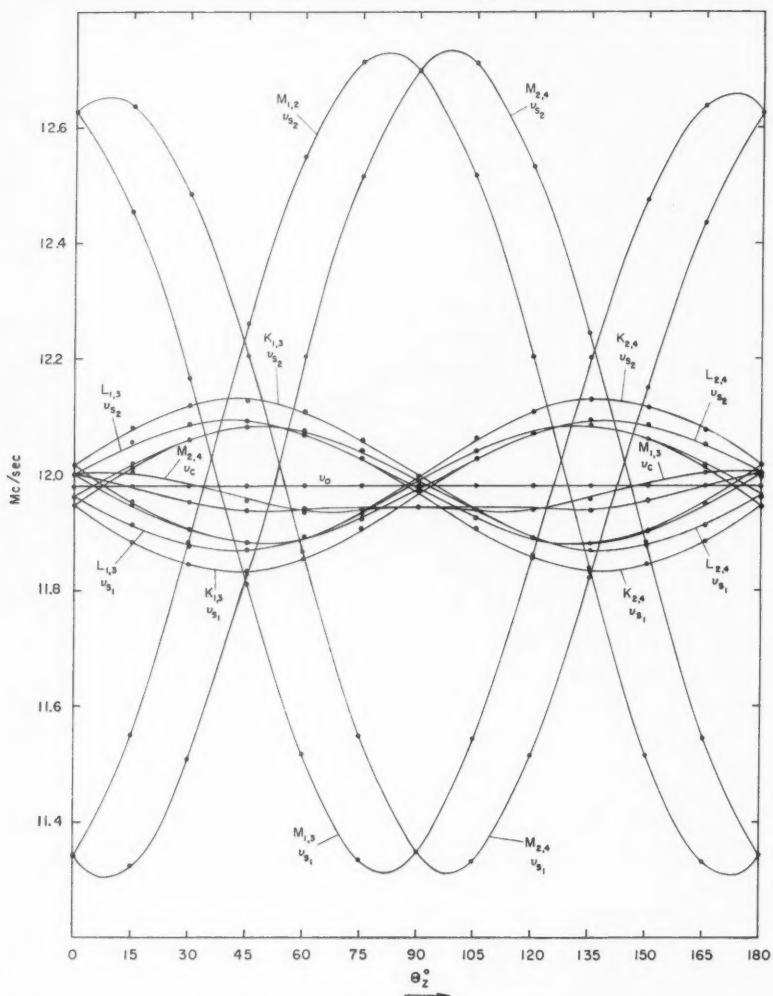
FIG. 5. The dependence on angular position of the B[11] resonance lines in colemanite at room temperature for the Z rotation.

four separate, but unresolved, central signals. The four lines denoted by $\nu^{M_{1\cdot3}}_{s_1}$, $\nu^{M_{1\cdot3}}_{s_2}$, $\nu^{M_{2\cdot4}}_{s_1}$, and $\nu^{M_{2\cdot4}}_{s_2}$ also occur in pairs with the two members of each pair *nearly* symmetrically situated with respect to ν_0. They must be satellite signals arising in two non-identical sets of sites. The quadrupole interactions at these sites must be strong because $\bar{\nu}$ is shifted from ν_0. Since the quadrupole interaction is so strong that $\bar{\nu}$ is shifted from ν_0, it is to be expected that the

frequencies of the central lines arising from the transitions $m = +1/2 \rightleftharpoons -1/2$ at these sites will also be shifted from ν_0. These central lines are clearly the remaining two lines denoted by $\nu_c^{M_{1,3}}$ and $\nu_c^{M_{2,4}}$ which always remain close in frequency to ν_0 but do not have symmetrically situated (with respect to ν_0) counterparts. Thus, after classification, the complex pattern of lines reveals itself as a superposition of six "simple" patterns.

In summary, the 15 lines occurring in the n.m.r. spectrum of B^{11} in colemanite at room temperature can be explained if one assumes the existence of six non-identical sets of boron sites per unit cell. The electric field gradients, which are large at two sites and small at the other four, must differ, in some respect, from one set of sites to another.

(b) The Point Group Symmetry of Colemanite at Room Temperature

Our next aim is to establish the point group symmetry of colemanite at room temperature. On the basis of chemical data and the unit cell dimensions, colemanite contains 12 boron atoms per unit cell. Remembering that two sites in a unit cell are identical from the point of view of the n.m.r. experiment only if they are related by a center of symmetry, it is apparent that colemanite, at room temperature, must have a centrosymmetrical structure since we have found that the 12 boron atoms occupy only six non-identical sites. Referring to Figs. 3, 4, and 5, it can be seen that the orientation patterns are symmetrical with respect to $\theta = 0°$ and $\theta = 90°$ in the X and Z rotations, and that the reduced spectrum occurs at the following positions: $\theta_X = 0°$ and $\theta_Z = 90°$ (Y, that is, b parallel to H_0), $\theta_X = 90°$ and $\theta_Z = 0°$ (Y perpendicular to H_0). Furthermore, as appears in Fig. 4, a reduced spectrum results for the complete Y rotation (b perpendicular to H_0). The reduction of distinguishable sites to three whenever the Y axis is either parallel or perpendicular to the magnetic field can be explained only if the Y axis is parallel either to a twofold (rotation or screw) axis or to a normal to a mirror (or glide) plane or to both. The combinations of these three alternatives with a center of symmetry all give the same point group symmetry $2/m$. Thus the 12 boron sites in the unit cell of colemanite at room temperature may be considered to have been derived by the operation of the symmetry group $2/m$ on the three unique boron sites in the asymmetric unit.

Actually, anticipating our low temperature results, the presence of 12 boron sites in the unit cell of colemanite, and hence of the center of symmetry at room temperature, can be established by the analysis of n.m.r. spectra alone. We shall return to this point later.

(c) Nomenclature for the Boron Sites and the Resonance Lines

The nomenclature of the boron sites and resonance lines was adopted with full regard paid to the fact that the established point group of colemanite at room temperature is $2/m$. The three sets of boron sites are designated by capital letters K, L, M, and the four symmetry-related sites making up each set are further identified by the subscripts 1,2, 3, and 4. Thus K_1 and K_2 are related by the twofold symmetry axis and so are K_3 and K_4. Since K_1 and K_3 (or K_2 and K_4) are related by the center of symmetry, ∇E at these sites are identical; hence at room temperature, these two sites are simply denoted

by $K_{1,3}$ (or $K_{2,4}$). The L and M sites are similarly denoted. The three lines arising from the transitions $m = \pm 3/2 \rightleftharpoons \pm 1/2$ and $m = +1/2 \rightleftharpoons -1/2$ are denoted by ν_{s_1}, ν_{s_2}, and ν_c respectively, the subscripts s_1 and s_2 being chosen to make $\Delta\nu = (\nu_{s_2} - \nu_{s_1})$ positive at $\theta_X = 0°$. The designation of each line is completed by attaching a superscript to indicate the site of its origin, thus $\nu_{s_1}^{M_{1,3}}$, $\nu_{s_2}^{M_{1,3}}$, $\nu_c^{M_{1,3}}$. Each line occurring in the reduced spectrum should be denoted by the superscript $P_{1,2,3,4}$ ($P = K$, L, or M) but, for brevity, it is denoted simply by the superscript P. The lines ν_c^K, ν_c^L in the Y rotation and $\nu_c^{K_{1,3}}$, $\nu_c^{K_{2,4}}$, $\nu_c^{L_{1,3}}$, and $\nu_c^{L_{2,4}}$ in the X and Z rotations are denoted simply by ν_0, since their frequencies are virtually identical with $\nu_0 = \mu H_0/Ih$.

(d) Quantitative Analysis of the B^{11} Spectrum

For a complete rotation of the crystal, the frequencies of the lines are predicted by theory to be periodic with a period of $180°$ and in fact the experimental points at $\theta°$ and $\theta°+180°$ in each case were found to differ by very little so they were averaged. The Fourier coefficients of the curves obtained for $\nu_{s_2} - \nu_{s_1}$, $\bar{\nu} - \nu_0$, and $\nu_c - \nu_0$ were determined by the 12-point analysis of Whittaker and Robinson (1948). The magnitudes of the coefficients for pairs, such as $P_{1,3}$ and $P_{2,4}$, which are related by the twofold screw axis (or the glide plane), were averaged because they possess numerically identical $\nabla \mathbf{E}$'s but their relative signs were retained because the $\nabla \mathbf{E}$'s differ in orientations of their principal axes. As expected theoretically, the coefficients of all terms involving angles other than 0, 2θ, and 4θ were found to be negligibly small. The other coefficients, labelled according to the nomenclature outlined in a previous section, are listed in Table I. Because of their greater accuracy, only the a, b, c coefficients were used in the determination of the

TABLE I

Averaged experimental values of the Fourier coefficients (in kc/sec) of the B^{11} lines in colemanite at room temperature

Sites	$K_{1,3},K_{2,4}$			$L_{1,3},L_{2,4}$			$M_{1,3},M_{2,4}$		
Rotation	X	Y	Z	X	Y	Z	X	Y	Z
$\nu_{s_2} - \nu_{s_1}$ a	$+22.5$	-7.8	-11.6	-36.5	-12.3	$+48.4$	$+641.3$	-675.7	$+32.4$
b	-6.0	$+30.0$	-26.7	$+63.5$	-83.9	$+22.6$	$+709.5$	$+609.2$	-1316
c	∓139.3	-299.3	∓209.8	∓44.7	$+130.0$	∓248.0	±1698	$+246.3$	∓404.1
$\bar{\nu} - \nu_0$ $\bar{n}$							$+26$	$+25$	$+33$
$\bar{p}$							$+0.8$	$+18$	-20
$\bar{r}$							±0.4	$+9$	∓6
$\bar{u}$							$+16$	-3	-11
$\bar{v}$							∓16	-2	∓7
$\nu_c - \nu_0$ n							-16	-6	-22
p							-6	-25	$+31$
r							∓14	$+13$	±9
u							-19	$+3$	$+13$
v							±19	-2	±8

NOTE: The two combinations of relative signs given for each set of coefficients refer to the two sets of sites (e.g., $K_{1,3}$ and $K_{2,4}$) related by the twofold screw axis. Experimental errors in the values of the a, b, c coefficients are about $+0.5$ kc/sec for the K sites and about ±1 kc/sec for the L and M sites. Experimental errors in the values of the n, p, r, u, v coefficients are about ±1.4 kc/sec.

tensor components ψ_{ij} in the X, Y, Z system which are shown in Table II. The relative signs of the off-diagonal components were not uniquely established by the a, b, c coefficients alone because of the fact that the Y rotation involved rotation about a twofold symmetry axis. In the case of the sites $M_{1,3}$ and $M_{2,4}$ the relative signs of the off-diagonal components could be determined simply from the signs of the coefficients obtained from the Fourier

TABLE II

Average values (in kc/sec) of the components of the tensor $\psi_{ij} \equiv eQ\phi_{ij}/h$, in the X, Y, Z co-ordinate system, for the B^{11} sites in colemanite at room temperatures

Sites	ψ_{XX}	ψ_{YY}	ψ_{ZZ}	ψ_{XY}	ψ_{YZ}	ψ_{ZX}
$K_{1,3}, K_{2,4}$	-38.0	$+15.3$	$+22.8$	± 210	± 139	$+299$
$L_{1,3}, L_{2,4}$	$+71.8$	$+25.8$	-97.6	± 248	± 44.7	-130
$M_{1,3}, M_{2,4}$	-1284	$+1350$	-66.5	± 404.1	∓ 1698	-246

NOTE: The two combinations of relative signs given for each set of tensor components refer to the two sets of sites (e.g., $K_{1,3}$ and $K_{2,4}$) related by the twofold screw axis. Experimental errors are about ± 1 kc/sec for the K sites and about ± 2 kc/sec for the L and M sites.

analyses of the separations of the centroids of the satellite frequencies from the unperturbed frequency. For the K and L sites, this simple procedure was not possible because the second-order effects were so small that the shifts of the centroids of the satellites could not be detected with the accuracy to which we worked. This problem was solved by making a few extra measurements at crystal orientations such that none of the X, Y, or Z axes were perpendicular or parallel to the magnetic field. The experimentally determined frequencies for these orientations were then compared with the values calculated on the basis of the two alternative combinations of signs for the off-diagonal components and the correct combination became apparent immediately.

The tensors, ψ_{ij}, were then diagonalized to yield the values for the quadrupole coupling constants and the asymmetry parameters listed in Table III. The

TABLE III

Quadrupole coupling constants and asymmetry parameters at the B^{11} sites in colemanite at room temperature and at $-40°$ C

Sites	Quadrupole coupling constant, Mc/sec		Asymmetry parameter	
	Room temperature	$-40°$ C	Room temperature	$-40°$ C
K_1, K_2	0.436 ± 0.001	0.421 ± 0.002	0.487 ± 0.002	0.566 ± 0.008
K_3, K_4		0.462 ± 0.002		0.433 ± 0.008
L_1, L_2	0.309 ± 0.001	0.259 ± 0.002	0.825 ± 0.003	0.862 ± 0.01
L_3, L_4		0.359 ± 0.002		0.793 ± 0.01
M_1, M_2	2.541 ± 0.004	2.522 ± 0.008	0.059 ± 0.003	0.087 ± 0.005
M_3, M_4		2.553 ± 0.008		0.022 ± 0.005

direction cosines of the principal axes of the ψ_{ij} tensors with respect to the X, Y, and Z axes are given in Table IV.

TABLE IV

Direction cosines, with respect to the X, Y, and Z axes, of the principal axes (x, y, z) of the electric field gradient tensors at the B^{11} sites in colemanite at room temperature

Sites	Reference axes	Principal axes		
		x	y	z
$K_{1,3}, K_{2,4}$	X	∓ 0.139	∓ 0.781	± 0.609
	Y	$+0.827$	$+0.247$	$+0.506$
	Z	∓ 0.545	± 0.574	± 0.611
$L_{1,3}, L_{2,4}$	X	± 0.258	± 0.603	∓ 0.755
	Y	-0.527	-0.567	-0.633
	Z	∓ 0.809	± 0.562	± 0.172
$M_{1,3}, M_{2,4}$	X	∓ 0.127	∓ 0.984	∓ 0.123
	Y	-0.536	$+0.173$	-0.826
	Z	∓ 0.834	± 0.040	± 0.550

NOTE: Only the relative signs within any given set of the above direction cosines are significant. The two combinations of relative signs given for each set of cosines refer to the two sets of sites (e.g., $K_{1,3}$ and $K_{2,4}$) related by the two-fold screw axis. The errors are about ± 0.001 in all the values.

2. Temperature Dependence of the B^{11} Resonance Lines

The primary purpose of this phase of the investigation was to find out whether n.m.r. techniques are sufficiently sensitive to detect phase transitions in which the atomic rearrangement is very small and, if so, to study the effect of the transition on the electric field gradients. It is known that some symmetry elements must be lost when the crystal transforms. The progress of a transition in which a symmetry element is lost can best be examined in colemanite by orienting the crystal with its b axis perpendicular to the magnetic field and observing the $m = \pm 3/2 \rightleftharpoons \pm 1/2$ transitions. Such an orientation has two advantages. Firstly, it can be made very accurately, to about 5 minutes of arc, by making use of our knowledge of the symmetry elements and the B^{11} spectrum. Secondly, the B^{11} nuclei within each group of symmetry-related sites appear to have identical surroundings, and therefore give rise to a single line for each of the $m = \pm 3/2 \rightleftharpoons \pm 1/2$ transitions as long as the point group symmetry is $2/m$ but as soon as one or more symmetry elements are lost each single line will split into two or four components (if they are all resolved). It should be possible to establish this splitting much more definitely than to establish a slight frequency shift in all the lines.

As the temperature is varied from about $+50°$ C down to about $+3°$ C, the boron resonance lines change by a very small amount in frequency but remain narrow indicating that the crystal rigorously maintains the point group $2/m$. In our earliest studies, we observed that at $0°$ C, each line starts to broaden rapidly and at about $-1°$ C it can be resolved into two distinct components. As the temperature is further decreased, the frequency separation between a pair of components, which originated from a common line, increases

until at about $-14°$ C, it reaches a value of about 18 kc/sec (for the M site at $\theta_Y = 149°$) after which it remains nearly constant until an additional effect, which will be discussed later, occurs. The above sequence of events appeared to be perfectly reversible and many thermal cycles such as described above had no measurable effect on the room temperature spectrum. The separations of the satellite lines (ν_{s_1} and ν_{s_2}) originating at the L and M sites for the orientation $\theta_Y = 149°$ are plotted as a function of temperature in Fig. 6. Separations between the satellites have been plotted rather than the
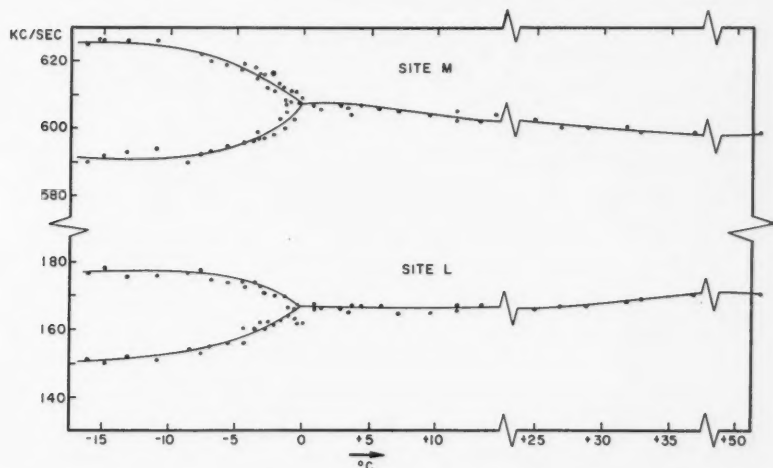

FIG. 6. Temperature dependences, in the region of the phase transition, of the separations between the satellite lines originating at the L and M sites. The crystal orientation was constant at $\theta_Y = 149°$.

frequencies of the satellites themselves because this emphasizes the change due to the transition and eliminates certain errors such as those due to slight changes in H_0. The fact that each satellite line splits into two components indicates that the center of symmetry has been lost but that the crystal retains either the twofold screw axis or the glide plane. In fact, as will be explained later, colemanite in this phase has the symmetry of point group 2.

During our detailed study (described in the next section) at $-40°$ C of colemanite in its phase with point group 2, we found that after a considerable time lapse each of the two components (of the original single line) is itself split into two subcomponents. This, as will be discussed later, has been taken to indicate the existence of a triclinic phase with the point group 1. The transformation to this triclinic phase was observed to occur at various temperatures below about $-30°$ C, the particular temperature at which the transformation occurs in a given case depending upon the immediate past thermal history of the crystal. Once this transformation has taken place, the crystal remains in its triclinic phase as the temperature is increased until,
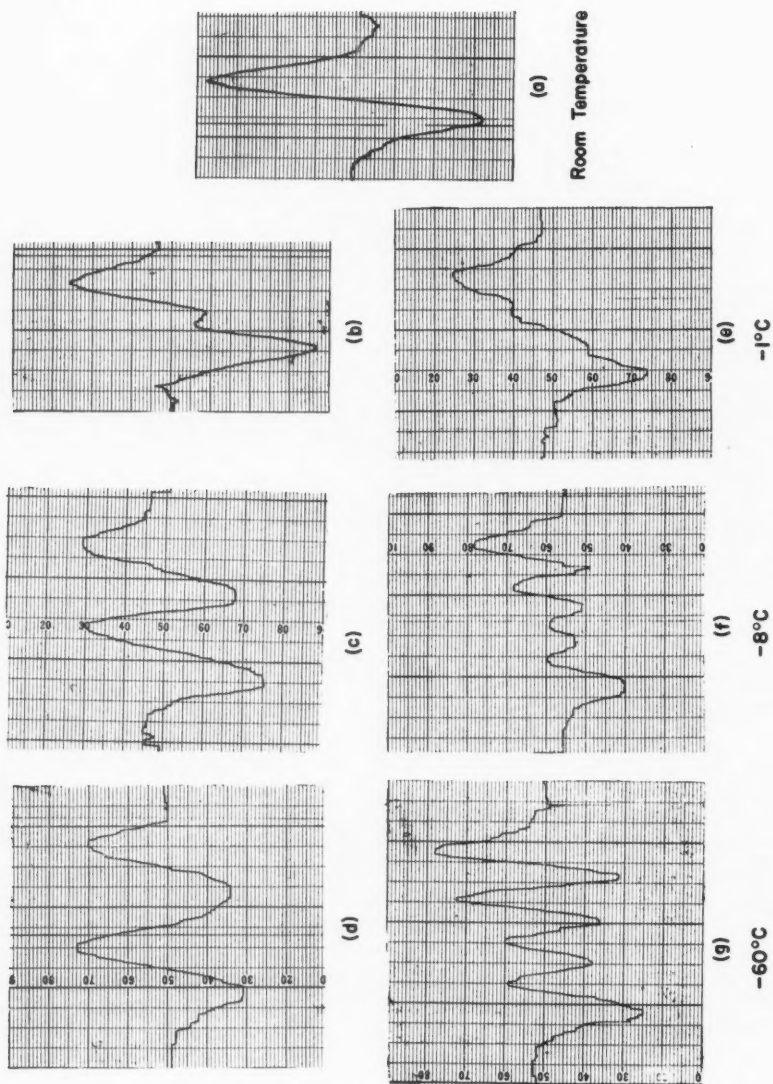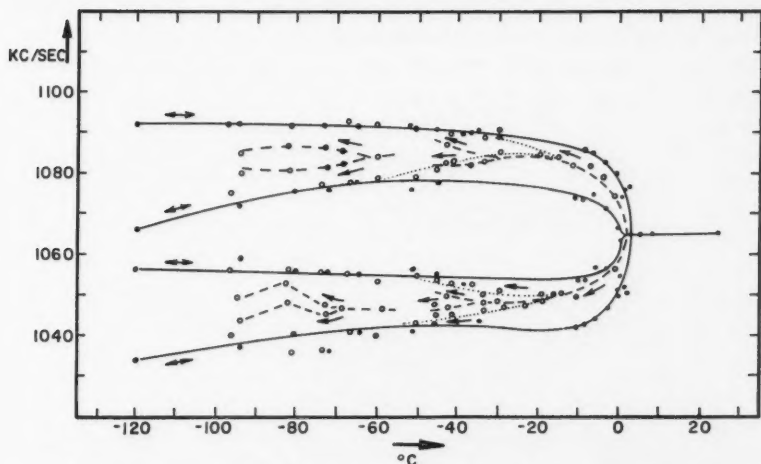
Fig. 7.

FIG. 8.   Temperature dependences of the separations between the satellite lines originating at the M site. The open circles with the dotted and dashed lines represent the separations as the crystal transformed first to the non-centrosymmetrical monoclinic phase and finally to the triclinic phase. The dots and solid lines give the separations as the crystal transformed directly to the triclinic phase. All separations were determined at a constant crystal orientation of $\theta_Y = 75°$.

in the region of 0° C, the four subcomponents, which were originally derived from a single line, again coalesce. However, the resulting single line is somewhat broader than it was before the thermal cycle and this increased breadth persists as the crystal is returned to room temperature. With the crystal maintained at room temperature, the widths of the resonance lines gradually decrease to their original values. If the crystal is then cooled, the transformations take place in the order described above. However, should it be cooled while the resonance lines are still broadened, the crystal transforms at about +3° C directly from the centrosymmetric to the triclinic phase which then persists to −120° C, the lowest temperature available to us. For the sake of comparison, Fig. 7 gives reproductions of the derivatives of an absorption line originating in an M site, taken first as the crystal transformed to the monoclinic phase and then, after the temperature had been recycled, as the crystal transformed to the triclinic phase. A plot of the frequency separation between the B^{11} satellite lines originating in the M sites is shown as a function of temperature in Fig. 8 for transformations to both the monoclinic and triclinic phases. Note that when the crystal transforms first to the monoclinic phase, the later transformation to the triclinic phase occurs at

FIG. 7.   The derivative of a B^{11} satellite line originating in an M site in colemanite recorded at selected temperatures with a constant crystal orientation of $\theta_Y = 75°$. (a), (b), (c), and (d) were recorded during the transformation to the non-centrosymmetrical monoclinic phase whereas (a), (e), (f), and (g) were recorded during the transformation to the triclinic phase. The frequency scale differs slightly from trace to trace but is about 4 kc/sec per chart division.

various temperatures. The splitting to the monoclinic phase was studied with a crystal orientation of $\theta_Y = 149°$ whereas the orientation $\theta_Y = 75°$ was used for the investigation of the transformation to the triclinic phase.

3. The B^{11} Spectrum of the Monoclinic Phase of Colemanite at −40° C

Figure 9A, a reproduction of a typical B^{11} spectrum in the monoclinic phase of colemanite at −40° C, shows very clearly, when it is compared with
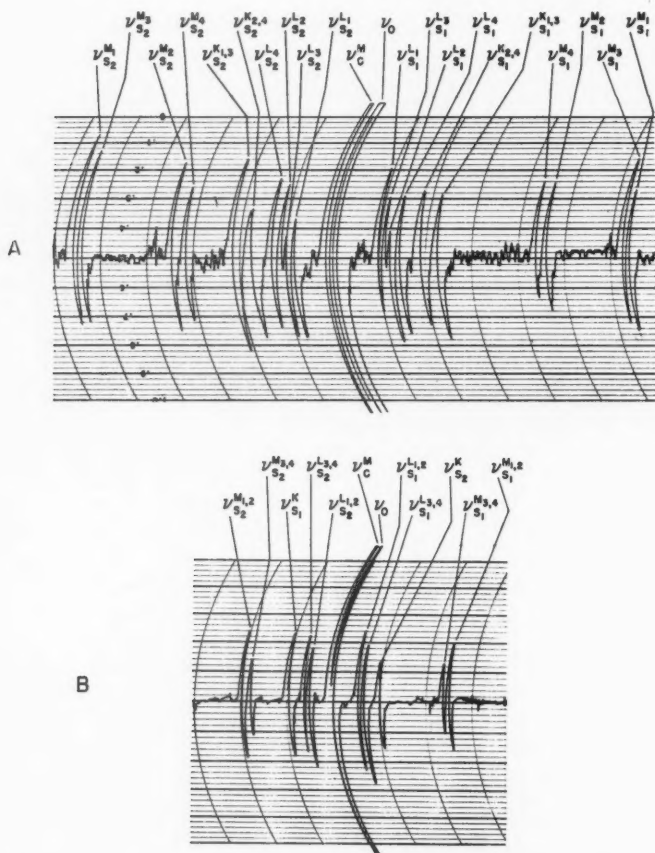
FIG. 9. Selected recordings of the derivatives of the B^{11} absorption lines in colemanite at −40° C.

(A) A typical spectrum obtained at −40° C. It was taken with a crystal orientation such that the X axis made an angle of 125° with H_0 and the Y and Z axes made angles of 4° and 94°, respectively, with the normal to the plane containing H_0 and the X axis. The frequency scale is approximately 71 kc/sec per chart division.

(B) An example of the reduced spectrum at −40° C obtained at the crystal orientation $\theta_Y = 150°$. The frequency scale is approximately 138 kc/sec per chart division.

Fig. 2A, that the center of symmetry has been lost. Note that all of the lines are not resolved at this particular orientation. As stated in the previous section a reduced spectrum is again obtained whenever the Y direction is parallel or perpendicular to the magnetic field. Such a reduced spectrum is shown in Fig. 9B and this is to be compared with Fig. 2B of the equivalent spectrum taken at room temperature. The frequencies of the lines for the three rotations have been plotted in Figs. 10, 11, and 12. Due to the need
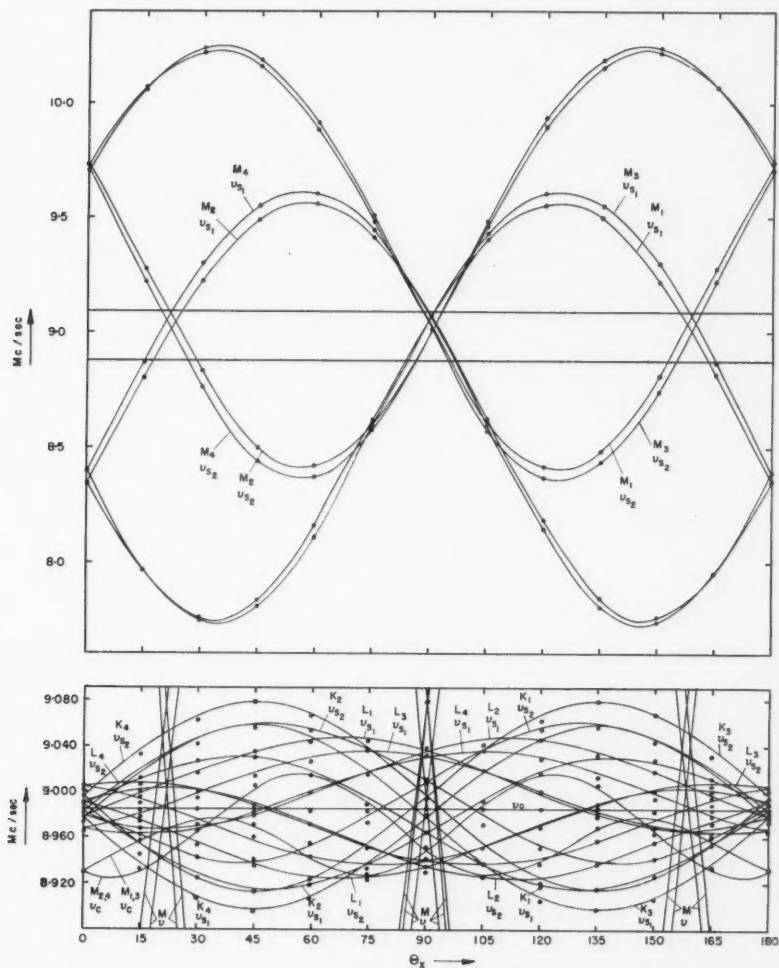
FIG. 10. The dependence on angular position of the B^{11} resonance lines in colemanite at $-40°$ C for the X rotation.
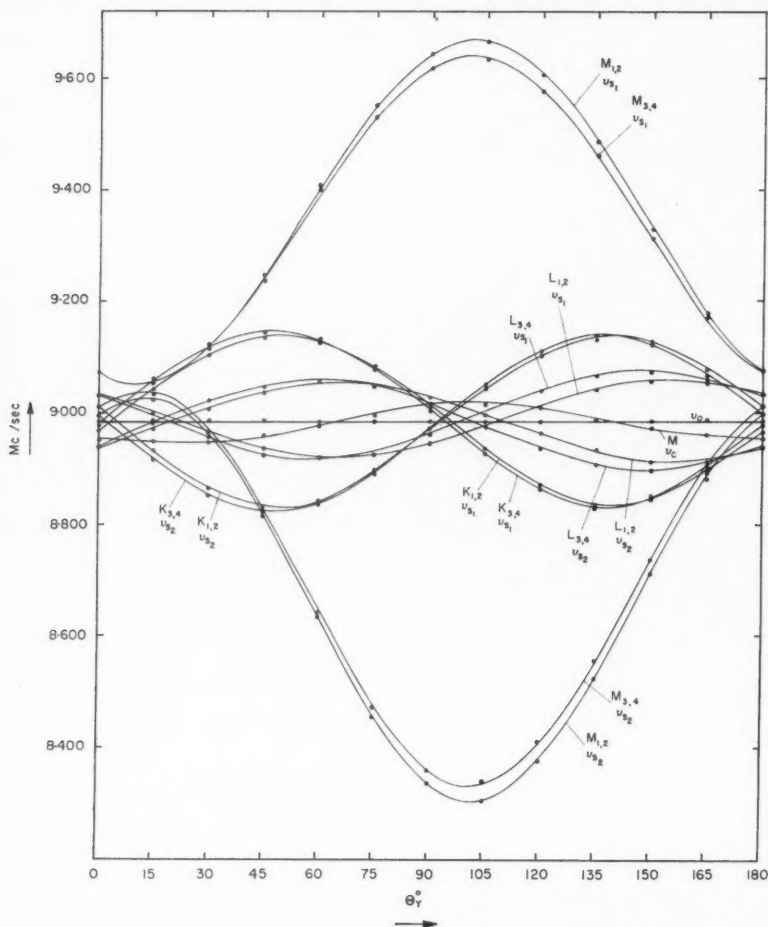
FIG. 11. The dependence on angular position of the B^{11} resonance lines in colemanite at $-40°$ C for the Y rotation.

for a larger gap to admit the cold cell, a less intense magnetic field was used in this investigation. Thus ν_0 was 8.985 Mc/sec for the work at $-40°$ C as compared with 11.981 Mc/sec for the work at room temperature. This change in ν_0 is of no consequence as far as this experiment is concerned because the Fourier coefficients a, b, and c are independent of ν_0, while n, p, r, u, and v, which vary inversely as ν_0, were not used except in the case of the M sites where only their signs were considered.

A comparison of Figs. 10, 11, and 12 with their room temperature counterparts reveals that each room temperature line, with the exception of ν_0 is
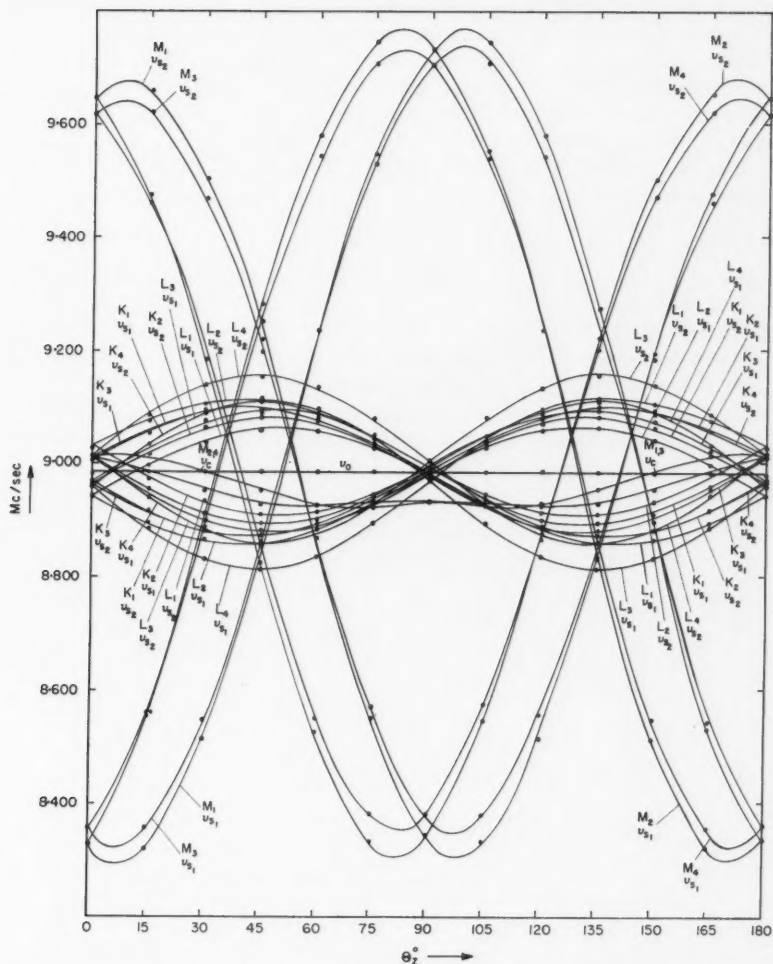
FIG. 12. The dependence on angular position of the B^{11} resonance lines in colemanite at $-40°$ C for the Z rotation.

split into two components as the crystal transforms. The separations between the components derived from $\nu_c^{M_{1,3}}$ and $\nu_c^{M_{2,4}}$ were so small that in general the components could not be resolved and appeared as two lines as shown in Figs. 10, 11, and 12 except at a few crystal orientations where the splitting could indeed be observed. The spectral lines at $-40°$ C can be classified in exactly the same way as in the room temperature case. It follows from such a classification that the n.m.r. spectrum in colemanite at $-40°$ C actually

contains 36 lines; only 27 of these lines are normally observed because eight central lines from the K and L sets are unresolved and appear as a single line at ν_0 and the four central lines from the M sites usually appear as only two lines. We conclude that the unit cell of colemanite in the monoclinic phase contains 12 boron sites at which the electric field gradients differ in some respect. Incidentally, the fact that there are 12 boron sites detectable by the n.m.r. method in this phase of colemanite as compared with the 6 sites detectable at room temperature confirms our earlier conclusion that colemanite is centrosymmetric at room temperature.

The quantitative analysis of the angular dependence of the n.m.r. lines has been performed in exactly the same way as that already described for the room temperature case. Since this phase of colemanite has point group 2, the pairs of sites P_1 and P_2 or P_3 and P_4 are related by the twofold axis and therefore possess numerically identical $\nabla \mathbf{E}$'s which differ only in the orientations of their principal axes. For this reason, the magnitudes of the Fourier coefficients for symmetry-related pairs have been averaged and are shown in Table V with their correct relative signs. As a consequence of the fact

TABLE V

Averaged experimental values of the Fourier coefficients (in kc/sec) of the B^{11} satellite lines in colemanite at $-40°$ C

Sites	Rotation	a	b	c
K_1,K_2	X	$+26.0$	-19.4	∓116.3
	Y	-1.7	$+45.4$	-300.2
	Z	-17.5	-22.4	∓203.7
K_3,K_4	X	$+18.5$	$+0.6$	∓161.3
	Y	-8.3	$+25.0$	-310.2
	Z	-6.1	-27.6	∓217.4
L_1,L_2	X	-43.9	$+56.9$	∓54.4
	Y	-5.6	-91.9	$+106.5$
	Z	$+49.0$	$+36.7$	∓199.1
L_3,L_4	X	-27.4	$+64.3$	∓32.8
	Y	-17.8	-73.5	$+141.3$
	Z	$+43.3$	$+10.8$	∓299.4
M_1,M_2	X	$+653.7$	$+733.3$	±1649.9
	Y	-695.4	$+614.3$	$+263.2$
	Z	$+37.6$	-1350.6	∓407.2
M_3,M_4	X	$+625.5$	$+699.4$	±1741.7
	Y	-660.3	$+597.7$	$+242.4$
	Z	$+32.4$	-1291.1	∓359.7

NOTE: The two combinations of relative signs given for each set of coefficients refer to the two sites (e.g., K_1 and K_2) related by the twofold screw axis. Experimental errors are about ±1.5 kc/sec.

that the Y rotation was taken about the symmetry axis, we again encountered the problem of assigning the appropriate signs to the off-diagonal components of ψ_{ij}. In the case of the M sites, a simple comparison of Figs. 10, 11, and 12 with their room temperature counterparts (Figs. 3, 4, and 5) shows that corresponding off-diagonal components must have the same sign. In the case

of the K and L sites, such a comparison did not give a completely unambiguous answer so one additional measurement was taken in order to establish the signs. The tensor components ψ_{ij}, listed for all the sites in Table VI, were diagonalized to yield the values for the quadrupole coupling constants and

TABLE VI

Average values (in kc/sec) of the components of the tensor $\psi_{ij} \equiv eQ\phi_{ij}/h$, in the X, Y, Z co-ordinate system, for the B^{11} sites in colemanite at $-40°$ C

Sites	ψ_{XX}	ψ_{YY}	ψ_{ZZ}	ψ_{XY}	ψ_{YZ}	ψ_{ZX}
K_1,K_2	-46.3	$+4.94$	$+41.4$	±204	±116	$+300$
K_3,K_4	-34.7	$+19.1$	$+15.6$	±217	±161	$+310$
L_1,L_2	$+86.6$	$+12.1$	-98.7	±199	±54.4	-107
L_3,L_4	$+54.9$	$+35.0$	-89.9	±299	±32.8	-141
M_1,M_2	-1310	$+1389$	-78.6	±407.2	∓1650	-263
M_3,M_4	-1256	$+1323$	-67.1	±360.0	∓1742	-242

NOTE: The two combinations of relative signs given for each set of tensor components refer to the two sites (e.g., K_1 and K_3) related by the twofold screw axis. Experimental errors are about ±3 kc/sec.

the asymmetry parameters. These have been listed in Table III to make convenient a comparison with the room temperature results. Table VII gives the direction cosines of the principal axes of the ψ_{ij} tensors with respect to the X, Y, and Z directions.

TABLE VII

Direction cosines, with respect to the X, Y, and Z axes, of the principal axes $(x. y, z)$ of the electric field gradient tensors at the B^{11} sites in colemanite at $-40°$ C

Sites	Reference axes	Principal axes		
		x	y	z
K_1,K_2	X	∓0.078	∓0.786	±0.613
	Y	$+0.830$	$+0.289$	$+0.476$
	Z	∓0.552	±0.546	±0.631
K_3,K_4	X	±0.184	±0.775	∓0.604
	Y	-0.831	-0.206	-0.517
	Z	±0.525	∓0.597	∓0.606
L_1,L_2	X	±0.295	±0.545	∓0.782
	Y	-0.566	-0.563	-0.606
	Z	∓0.770	±0.622	±0.142
L_3,L_4	X	∓0.208	∓0.649	±0.731
	Y	$+0.469$	$+0.590$	$+0.657$
	Z	±0.858	∓0.480	∓0.182
M_1,M_2	X	∓0.005	∓0.992	∓0.125
	Y	-0.544	$+0.116$	-0.831
	Z	∓0.838	±0.050	±0.542
M_3,M_4	X	±0.018	±0.993	±0.113
	Y	$+0.559$	-0.103	$+0.823$
	Z	±0.829	∓0.050	∓0.557

NOTE: The two combinations of relative signs given for each set of cosines refer to the two sites (e.g., K_1 and K_3) related by the twofold screw axis. The errors are about ±0.002 in the values for the K and M sites, and about ±0.003 in the values for the L sites.

4. Proton Resonance Line Width

We have carried out a preliminary study of the temperature dependence of the proton line width in colemanite to test the suggestion made by Christ, Clark, and Evans (1958) that the ferroelectric behavior of colemanite can be traced to an ordering of certain hydrogen bonds which they believe to be in a state of dynamic disorder in the room temperature phase. If their suggestion is correct, one would expect a broadening of the proton resonance signal at the transition temperature.

The second moment of the proton signal is plotted as a function of crystal temperature in Fig. 13. Within our experimental accuracy, the second moment did not depend on whether the crystal transformed to the monoclinic or the triclinic phase, as indicated by the B^{11} signals, so the results have all been plotted in Fig. 13. This plot shows clearly that the proton signal, which
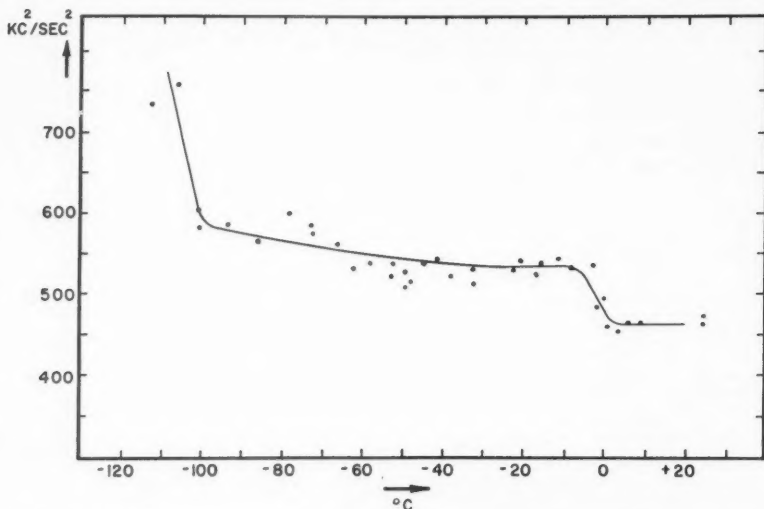

FIG. 13. Temperature dependence of the second moment of the proton resonance line in colemanite. The experimental error associated with each point is about ± 35 kc²/sec².

is rather complex, does begin to broaden rather abruptly in the region of 0° C. As the temperature is further decreased, the proton signal continues to broaden very slowly until in the region of about −100° C it again broadens abruptly. There is also some suggestion of a small abrupt broadening of the signal in the region of −70° C but the experimental accuracy was not good enough to decide this point.

DISCUSSION

The symmetry properties of colemanite in its different phases have been studied by other workers using various techniques. The X-ray diffraction

study of Christ, Clark, and Evans (1958) showed that a centrosymmetric structure prevails at room temperature and they were unable to find the slightest indication of any departure from the space group $P2_1/a$, even on greatly overexposed films. From a study of the patterns formed by electrical breakdown paths, Davisson (1956) concluded that colemanite shows the symmetry of point group $2/m$ at 150° C and 30° C, and perhaps also at −195° C. He found, however, that colemanite is both pyroelectric and piezo-electric. His plot of the pyroelectric constant against temperature gave a high and narrow peak at −2.5° C with an appreciable tail on the low-tempera-ture side and a small and rapidly decreasing value for the constant on the high-temperature side. Davisson's conclusion was that the essential framework of the crystal remains centrosymmetrical at all temperatures and that the asymmetry may be due to slight displacements of certain constituents, presumably the light atoms, from centrosymmetrical positions. Chynoweth (1957) has also measured the pyroelectric properties of colemanite and found a second-order transition at −6° C to a ferroelectric phase. He concluded, however, in disagreement with Davisson, that at temperatures higher than about −5 °C an ideal single crystal of colemanite would show no pyroelectric effect and is centrosymmetrical above this temperature.

In our own work we have found that the unit cell of colemanite contains 12 non-identical boron sites at temperatures below 0° C but only 6 distinguish-able sites above 0° C. This indicates in a quite unambiguous manner that the room temperature phase is centrosymmetrical in agreement with the conclusions of Christ *et al.* and Chynoweth. The combination of the center of symmetry with the twofold axis and/or the plane of symmetry gives the point group as $2/m$ which is consistent with the space group $P2_1/a$ as deter-mined by X-ray analysis.

If, as suggested by Christ *et al.*, there is an ordering of hydrogen bonds at the transition, we would expect the space group symmetry to be reduced either to $P2_1$ or to Pa and possibly to $P1$ but no prediction can be made on the basis of the structure determination alone. In the ferroelectric phase the polar axis must be parallel to the b axis if the space group is $P2_1$ and per-pendicular to the b axis if the space group is Pa but it may have any orientation if the space group is $P1$. Davisson, Goldsmith (1956), and Chynoweth all found the polar axis to be parallel to the b axis which rules out the possibility of Pa. It does not entirely rule out the possibility of $P1$ because the departure of the polar axis from parallelism with the b axis may be too slight, of the order of a few minutes of arc, to be detected by the techniques used by the above workers. Our work demonstrates quite clearly that colemanite may transform into a phase in which only 6 of the 12 boron sites are unique and this rules out, for this particular phase, the possibility of $P1$. Thus, at temperatures below about 0° C, colemanite has a phase which possesses the space group $P2_1$. This is in agreement with some recent X-ray work of Black and Burley, of the U.S. National Bureau of Standards (reported by Christ, Clark, and Evans (1958)).

As reported in an earlier section, we have observed that, with the colemanite crystal oriented with its b axis perpendicular to the magnetic field, a single resonance line, arising from the same nuclear transition at the four symmetry-related sites in the room temperature phase, may split into two components or, under certain conditions, into four components as the temperature is decreased below about 0° C. The case where it splits into two components is quite unambiguous and has been discussed in the previous paragraph. There are three possible mechanisms which would lead to the single line splitting into four components. The first possibility is that the crystal has transformed into the monoclinic phase with the space group P2₁ and at the same time the crystal has become misaligned so that the symmetry axis (b axis) is no longer perpendicular to the magnetic field. This would be a simple instrumental difficulty and of no interest. After numerous tests, all of which indicated that the crystal had not become misaligned, we feel 90% certain that this possibility can be discarded. The second possibility is that the crystal has transformed into the phase with space group P2₁ and at the same time twinned. This very often happens when a ferroelectric crystal transforms. If such were the case, we would expect the four components to be further split into at least eight components as soon as the b axis is tilted from its position perpendicular to the magnetic field. The four components were studied at various arbitrary crystal orientations but no additional splitting ever appeared. The remaining possibility is that the crystal has transformed into a heretofore unreported phase with the space group P1. The orientation of this new phase is not uniquely determined by the orientation of the preceding room temperature phase as we sometimes observed the maximum splitting at about $\theta_Y = 79°$ with a minimum about $\theta_Y = 150°$ whereas after another temperature recycle the minimum splitting would sometimes occur at about $\theta_Y = 79°$ with the maximum at about $\theta_Y = 150°$. These angles could not be determined very precisely as the total splitting is very small and changes very slowly with angle.

It thus appears that the monoclinic phase is actually metastable with respect to a triclinic phase. The activation energies associated with these transitions would be very small indeed but apparently the monoclinic phase is slightly favored. We think it very likely that the triclinic phase is also ferroelectric and that the existence of these two alternate phases may offer a partial explanation for the variety of behaviors reported by Wieder (1959) for different samples of colemanite.

Let us now discuss the phase transition. As the temperature approaches that of the transition, a selected signal broadens rather slowly which implies a very small unresolved splitting, then splits into two (or four) components. The separation between the components increases fairly rapidly at first and then approaches a value which remains nearly constant as the temperature is further reduced. Such behavior is illustrated in Figs. 6 and 8. It should be noted in particular that the changes in the n.m.r. spectrum occurring at the transition are not due to a gradual growth of the signals arising in the new phase at the expense of the signal belonging to the centrosymmetric

phase. The smooth manner in which the lines split as the crystal transforms suggests that the entire crystal transforms at once and that just at the transition temperature (which cannot, by its very nature, be exactly determined) the atomic arrangement in either of the low-temperature phases is virtually identical with that of the room temperature phase. As the temperature is lowered below that of the transition, the atomic configuration rearranges itself until a stable arrangement is reached which then changes very little as the temperature is further reduced. This behavior is very much what we would expect of a second-order displacive transition.

The question remains as to whether this splitting is due to an actual rearrangement of the boron–oxygen configuration or whether it simply is a reflection of an ordering of the hydrogen bonds. Since the broadening of the proton line begins at the same temperature as the splitting in the B^{11} resonance lines, there seems little doubt that the two effects are connected. Because the temperature dependence of the broadening of the proton lines is the same whether the crystal, as indicated by the B^{11} spectra, transforms to the triclinic or monoclinic phase and is so different from the temperature dependence of the splitting of the boron lines, we believe that two different mechanisms are involved: probably the initial ordering of the hydrogen bonds removes a constraint so that a reorientation of the boron–oxygen arrangement to a slightly more stable configuration becomes possible. In other words, the ordering of the hydrogen bonds may be said to trigger the reorientation of the boron–oxygen configuration. The broadening of the proton line is probably due to the ordering of at least two groups of hydrogen bonds and it may be argued that the splitting of the B^{11} lines reflects ordering of one type of hydrogen bond but that the other type of hydrogen bond is too far away or not intimately enough connected to cause any effect at the boron sites, thus explaining the difference between the temperature dependences of the proton and B^{11} spectra. According to the system of hydrogen bonds proposed by Christ *et al.*, ordering is possible for the hydroxyl group O_6 and likely for the water molecules, O_8. Any ordering of the O_6 group would be expected to affect the boron atoms most strongly since O_6 forms part of the boron–oxygen chain. O_8 is connected to the boron–oxygen chain only through hydrogen bonding to one of the oxygen atoms, O_7. Thus if we were to miss the effects of an ordering process among these hydrogen bonds we would expect it to be the one involving the water molecules; yet Christ *et al.* feel most strongly that this is the very ordering process which leads to the ferroelectric behavior and therefore it must occur at about $0°$ C where we observe the major effect on the B^{11} lines. It is possible that a thorough study of the complex proton resonance will help to clarify this point.

In principle, it should be possible to use the quantitative data on the B^{11} quadrupole coupling tensors in the room temperature and ferroelectric phases, to derive the structural changes which take place at the transition. However, the computational procedures are likely to be prohibitively difficult since in this case, one cannot use a simple model of point charges. It is likely that information about the structural changes can best be obtained by a neutron

diffraction study of colemanite although an additional difficulty, that of the high-absorption cross section of the B^{10} nuclei for thermal neutrons, will be encountered.

The transition temperature of colemanite has been variously reported as $-2.5°$ C (Goldsmith 1956), $-6°$ C (Chynoweth 1957), and $-7°$ C (Wieder 1959). We have found that in our crystal the transition occurs at a temperature several degrees higher than any of these values but there is probably little significance to this variation. Wieder reported finding a wide variation in transition temperatures, between $-7°$ C and $0°$ C for a number of samples, which he attributed to internal space changes caused by impurities. Samples from the same collection of colemanite from which our crystal was taken give biased hysteresis loops which suggest that the transition in our crystal may have been elevated by space charge effects. One interesting point regarding the transition temperature is the fact that we observed the transition to the triclinic phase to take place at a consistently higher temperature, $3°$ C, than the transition to the monoclinic phase at $0°$ C. This suggests that two separate transitions are involved which fortuitously occur very close together and if the room temperature phase happens to be undercooled below the temperature of the first transition it transforms directly to the monoclinic phase which is metastable. It can of course be argued that we cannot define an exact transition temperature because of the very nature of the transition and that we simply observe the change to the triclinic phase at a higher temperature because the final splitting is larger than in the monoclinic case. Following this argument, there is only one transition with two alternatives, but only slightly different, boron–oxygen configurations available to the structure. The first broadening of the proton line is not abrupt enough for us to be able to set a sufficiently small error on the transition temperature to help distinguish between the two alternatives and we have been unable to settle the point.

To a certain extent, one may correlate the boron sites, as determined by the n.m.r. results, with the structural co-ordination of the boron atoms. In the discussion to follow it will be assumed that only nearest neighbors make significant contributions to ∇E at a boron site. Christ *et al.* have shown that two of the three boron atoms in the asymmetric unit (at room temperature) are located in the interstitial positions near the centers of two slightly distorted oxygen tetrahedra and that the third occupies the interstitial position at the center of a slightly distorted equilateral triangle of oxygen atoms. At the center of a perfect tetrahedron the symmetry is cubic so that ∇E must be zero. In a slightly distorted tetrahedron, however, one would expect the magnitude of ∇E and therefore the quadrupole coupling constant to be small at the center although it need no longer be zero. Without a detailed knowledge of the distortion and resulting charge density distribution one cannot predict the orientation of the principal axes of ∇E nor the value of η, the asymmetry parameter. The symmetry at the center of a perfect equilateral triangle requires that η be zero and that the z principal axis be parallel to the normal to the plane of the triangle but puts no restriction on the magnitude of ∇E. Thus in the case of the BO_3 triangle, we would expect the quadrupole coupling

constant to be considerably larger than for the BO_4 tetrahedra and, unless the triangle is greatly distorted, that the value of η should be small and that the z principal axis should be nearly perpendicular to the plane containing the three oxygen atoms. As shown in Table III, we have indeed found that the quadrupole coupling constants are small at the K and L boron sites, whereas the quadrupole coupling constant is considerably larger and η is very small at the M site. Also, it follows from the atomic co-ordinates (Christ *et al.* 1958) that the z principal axis of the electric quadrupole coupling tensor at the M site is nearly parallel to the normal to the plane containing the oxygens (O_1, O_2, and O_4 in Fig. 1) in the triangle. This is clearly shown by the direction cosines with respect to the $\mathbf{b} \times \mathbf{c}$, $\mathbf{b}$, and $\mathbf{c}$ directions, respectively, shown below:

direction cosines of z principal axis

$$\pm 0 \cdot 123 \pm 0 \cdot 001 \qquad \mp 0 \cdot 826 \pm 0 \cdot 001 \qquad \mp 0 \cdot 550 \pm 0 \cdot 001,$$

direction cosines of normal to plane

$$\pm 0 \cdot 109 \qquad\qquad \mp 0 \cdot 843 \qquad\qquad \mp 0 \cdot 527.$$

There seems little doubt that the boron sites which we have labelled K and L are in the oxygen tetrahedra and that the M site is in the oxygen triangle. We have been unable to find an unambiguous correlation between our K and L sites and the individual boron sites in the tetrahedra.

Incidentally, it is of interest to note that the n.m.r. study of the boron sites in kernite (Waterman and Volkoff 1955) revealed that the electric field gradients existing at sites C and D (using Waterman and Volkoff's nomenclature) are very similar to those at our sites K and L, while the electric fields existing at boron sites E and F are very similar to those at our site M. A

TABLE VIII

A comparison of the values obtained by Waterman and Volkoff for the quadrupole coupling constants and asymmetry parameters for the B^{11} sites in kernite with the values obtained for colemanite at room temperature

Kernite sites	C	D	E	F	Colemanite sites	K	L	M
Quadrupole coupling constant, kc/sec	645	588	2563	2567	Quadrupole coupling constant, kc/sec	436	309	2541
Asymmetry parameter	0.54	0.60	0.163	0.117	Asymmetry parameter	0.487	0.825	0.059

comparison is given in Table VIII. In view of this striking similarity, we suggest that kernite contains two BO_4 tetrahedra and two BO_3 triangles, contrary to the X-ray analysis results of Portoles (1948). This suggestion has been supported by Dr. Christ (private communication), who has pointed out that the boron–oxygen chains should be the same in kernite as in borax. Morimoto (1956) has shown that borax, which has the same chemical formula as kernite except for the water of hydration, contains two BO_4 tetrahedra and two BO_3 triangles in its asymmetric unit.

ACKNOWLEDGMENTS

REFERENCES

ANDREW, E. R. 1955. Nuclear magnetic resonance (Cambridge University Press, Cambridge).
CHRIST, C. L. 1953. Am. Mineralogist, **38**, 411.
CHRIST, C. L., CLARK, J. R., and EVANS, H. T., Jr. 1958. Acta Cryst. **11**, 761.
CHYNOWETH, A. G. 1957. Acta Cryst. **10**, 511.
DAVISSON, J. W. 1956. Acta Cryst. **9**, 9.
GOLDSMITH, G. J. 1956. Bull. Am. Phys. Soc. Ser. II, **1**, 322.
MORIMOTO, N. 1956. Min. (Japan) **2**, 1.
PORTOLES, L. 1948. Estud. Geol. Inst. Mallada, **7**, 21.
POUND, R. W. 1950. Phys. Rev. **79**, 685.
SCHUSTER, N. A. 1951. Rev. Sci. Instr. **22**, 254.
VANVLECK, J. H. 1948. Phys. Rev. **74**, 1168.
VOLKOFF, G. M. 1953. Can. J. Phys. **31**, 820.
VOLKOFF, G. M., PETCH, H. E., and SMELLIE, D. W. L. 1952. Can. J. Phys. **30**, 270.
WATERMAN, H. H. and VOLKOFF, G. M. 1955. Can. J. Phys. **33**, 156.
WHITTAKER, E. and ROBINSON, G. 1948. The calculus of observations (Blackie and Son Ltd., London).
WIEDER, H. H. 1959. J. Appl. Phys. **30**, 1010.

RELATIVE ENERGIES OF TILT-TYPE
SUBBOUNDARIES IN ALUMINUM[1]

K. T. Aust

ABSTRACT

The relative energies of subboundaries were obtained, in terms of a reference large-angle grain boundary, in aluminum bicrystals having two different effective impurity concentrations. The data for subboundary energy versus subgrain orientation difference (θ) showed a cusp at $\theta \simeq 0.75°$. The existence of such a cusp was previously predicted by Martius and Chalmers from considerations of impurity effects at boundaries.

INTRODUCTION

During a study of grain boundary migration motivated by subboundaries in bicrystals of aluminum (Aust 1959), it became apparent that the relative energies of the subboundaries could be obtained in terms of the grain boundary. The method consisted of measuring the dihedral grain boundary angle at the point of intersection of each subboundary with the grain boundary, after annealing near the melting point of the metal. The results, to be described in this report, indicate the presence of an energy cusp at an orientation difference of about 0.75°. The existence of such a cusp was previously predicted by Martius and Chalmers (1952) on the basis of impurity effects at boundaries. This observation is believed to represent the first experimentally measured energy cusp for interfaces, except for those existing at twin boundaries. Several of the consequences of this phenomenon, in relation to properties of boundaries in metals, are discussed.

EXPERIMENTAL PROCEDURE AND OBSERVATIONS

Single crystals of zone-refined aluminum, approximately 1 cm sq. and 37 cm in length, were obtained by zone-melting aluminum of 99.996 wt.% starting purity in a graphite boat under helium atmosphere. A molten zone of 2 to 3 cm in length, which was maintained by induction heating, was passed along the length of the bar usually at a rate of 0.9 mm per minute, except the last pass in which the rate was 0.2 mm per minute. Two single-crystal specimens having different impurity contents were produced by passing the molten zone along the entire length of the bar for 4 passes in one case and 12 passes in another.

Direct measurements on the 4-pass and 12-pass aluminum single crystals using the method of Bean, DeBlois, and Nesbitt (1959) gave the following data for the resistance ratio between the electrical resistance at room temperature and the resistance at liquid helium temperature:

$$\frac{R\,298°\,K}{R\,4.2°\,K},$$

4-pass Al crystal, center of bar   3100,

12-pass Al crystal, center of bar   9000.

The resistivity ratio for the center portion of the 12-pass aluminum may be the highest yet reported for aluminum, but still represents an effective impurity content of a few parts per million. In addition, the thermally activated motion of grain boundaries, which is known to be very sensitive to solute impurity content (Rutter and Aust 1958), was also studied. It was found that the velocity of grain boundaries was 1 to 2 orders of magnitude faster, and with a much smaller temperature dependence, in the case of the 12-pass aluminum as compared with the 4-pass aluminum (Aust 1959).

It is evident from both the electrical resistivity and grain boundary migration experiments that the effective impurity content of the 12-pass aluminum crystal is less than that of the 4-pass crystal.

Single crystals of about 4 cm in length were removed from the center portion of each zone-refined bar by cutting them with a jeweller's saw, then etching them in aqua regia to remove any strained material at the cut surfaces. The single crystals were electrolytically polished in a 2:1 solution of methyl alcohol and concentrated nitric acid, using intermittent polishing periods for a total time of 30 to 40 minutes at a current density of 10 amp per sq. dm. The specimens were then chemically polished in Alcoa R-5 solution. X-Ray and micrographic studies indicated the presence of striations or lineage sub-structure in the single crystals, having misorientations as high as 2°. The orientations of the 4-pass and 12-pass aluminum single crystals, containing substructure, are given in Fig. 1.
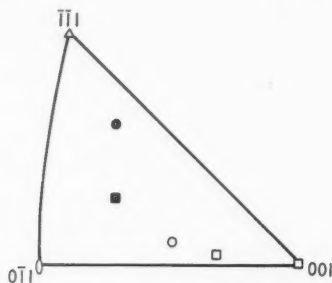

FIG. 1. Stereographic plot of specimen axis or growth direction (○ ●) and normal to top surface (□ ■) of starting single crystals; 4-pass Al (light) and 12-pass Al (shaded).

Bicrystal specimens, containing one crystal with lineage and the other crystal without lineage, were next obtained from the single crystals using the following technique, previously described by Rutter and Aust (1958, 1959). One end of the striated single crystal was deformed locally in compression and the specimen then annealed in argon at 600–640° C. Numerous new recrystal-lized grains are thereby introduced at one end of the specimen, from which it is sometimes found that one recrystallized grain grows preferentially into the lineage substructure of the undeformed part of the crystal. In this way, it was possible to obtain a single grain produced by recrystallization growing into a striated melt-grown crystal. Figure 2 shows an example of such growth in the 12-pass aluminum.

PLATE I

FIG. 2. Macrophotograph showing growth of a new recrystallized grain into a striated crystal in 12-pass Al. 10X.
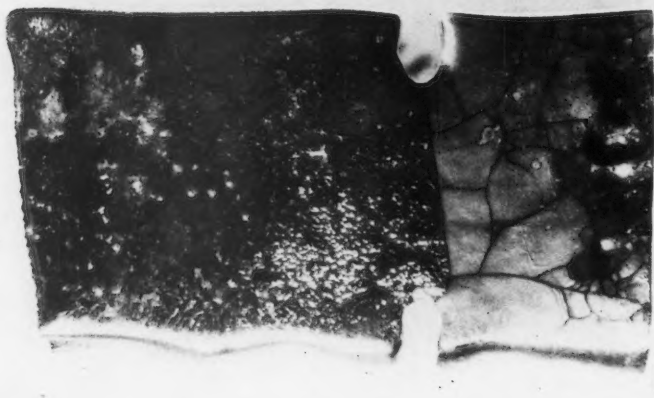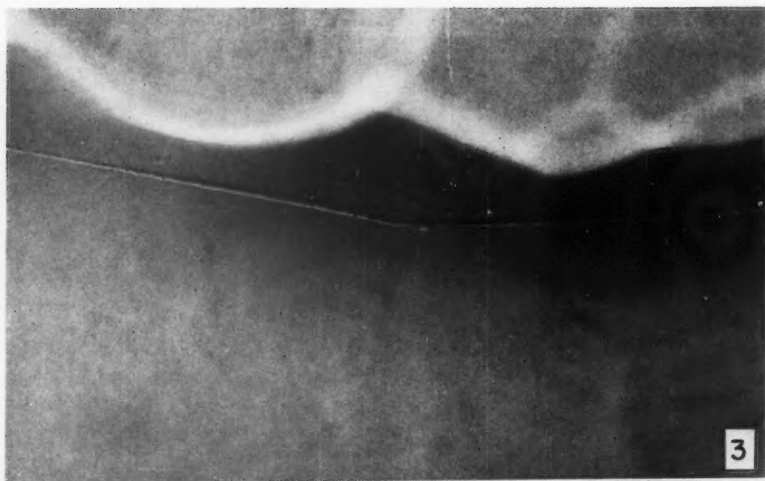
PLATE II

FIG. 3. Photomicrograph showing grain boundary – subboundary interaction. 1000×.
FIG. 4. Macrophotograph showing anchored grain boundary in 4-pass Al bicrystal. 5.5×.

The orientation differences of the subboundaries, such as depicted in Fig. 2, were obtained to an accuracy of ±.05° by positioning an X-ray beam on the subboundary and thereby recording the Laue reflections from two adjacent subgrains on the same film. Analysis of the X-ray Laue back-reflection films revealed that the subboundaries, which run nearly horizontally (Fig. 2) and which intersect the grain boundary, were tilt-type boundaries having mis-orientations of 0.1 to 2°. Several of the subboundaries which are approximately vertical (Fig. 2) were also analyzed and found to be twist-type boundaries, with misorientations of the order of 0.5°.

The bicrystals were chemically polished prior to each argon anneal, and the interfaces were clearly revealed by thermal etching as seen in Fig. 2. Each triple point, where a tilt-type subboundary intersected the grain boundary, was photographed at ×500 to ×1000 after several annealing treatments at 640° C in argon. The dihedral angle, e, made by the grain boundary at each point of intersection with a subboundary, was measured to within ±0.5°, directly from the negatives or from prints enlarged up to 4 times the original magnification. A typical example of a grain boundary–subboundary interaction is shown in Fig. 3. The relative energies of the tilt-type subboundaries were obtained in terms of the reference grain boundary, to an accuracy of ±.01, using the relationship

$$(1) \qquad\qquad \gamma s/\gamma G = 2 \cos (e/2)$$

where γs is the energy of the subboundary, γG is the energy of the reference grain boundary, and e is the dihedral angle opposite the subboundary. A measurement of e then yields the value of γs, when γG is assumed to equal unity. The angle e varied from 165° to 179.5°, resulting in values of γs from 0.26 to 0.01.

The relative energy of the subboundaries (γs) as a function of the subgrain orientation difference (θ) was obtained for two bicrystal specimens, one from the 4-pass aluminum and the other from the 12-pass aluminum. The orientation differences of the two reference large-angle grain boundaries are given in Fig. 5, where the single axis relating the starting striated crystal with the adjacent recrystallized grain by the smallest amount of rotation (α) is plotted.
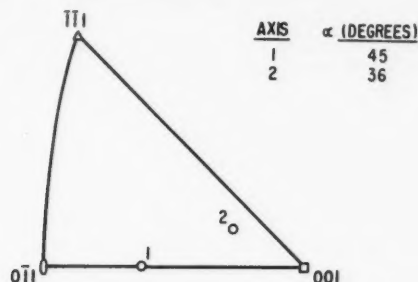

FIG. 5. Orientation relationships for the two bicrystals. 4-pass Al, axis 1; 12-pass Al, axis 2.

RESULTS AND DISCUSSION

The results obtained for the relative energy of the subboundaries (γs) in terms of a large-angle grain boundary, as a function of orientation difference (θ) of the subgrains, are shown in Figs. 6 and 7 for the 4-pass and 12-pass aluminum bicrystals respectively. The two curves are similar in that γs
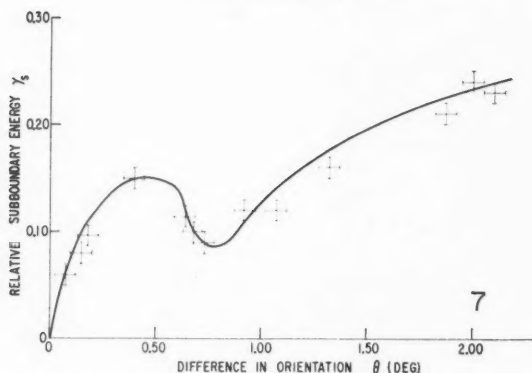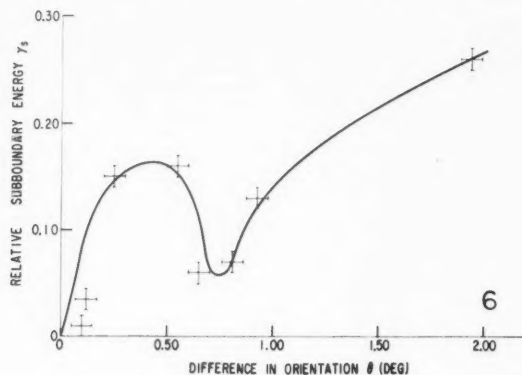

FIG. 6. Relative subboundary energy versus orientation difference of the subgrains in 4-pass Al.
FIG. 7. Relative subboundary energy versus orientation difference of the subgrains in 12-pass Al.

rises rapidly with increasing θ, reaching a maximum value of 0.15–0.16 at $\theta = 0.4$–$0.5°$; γs drops with further increase in θ, reaching a minimum value at $\theta = 0.7$–$0.8°$, and then increases again with further increase in θ. The main difference in the two curves of Figs. 6 and 7 is the relative drop in γs from 0.16 to 0.06 for the 4-pass aluminum, and from 0.15 to 0.09 for the 12-pass aluminum, i.e., a slightly more pronounced energy cusp is present in the aluminum bicrystal of lower purity.

The results depicted in Figs. 6 and 7 were obtained under essentially dynamic conditions where the subboundaries provided the driving force for the motion of the grain boundary. In order to determine whether this data represented equilibrium values of γs (where equation (1) is only applicable), the following experiment was conducted. Grooves were acid-cut on opposite sides of the 4-pass aluminum bicrystal, just ahead of the moving grain boundary. The specimen was then annealed at 640° C in argon until the grain boundary became anchored in the grooves, reaching an equilibrium position in which the lineage driving energy was balanced by an equal and opposite driving energy associated with the energy and curvature of the grain boundary. Figure 4 shows the anchored grain boundary in equilibrium condition after annealing at 640° C for 5 hours. Two of the grain boundary dihedral angles, at points of intersection with the subboundaries, were then remeasured and the relative energy of the subboundaries obtained from equation (1) as before. The results for the 4-pass specimen were as follows:

θ (deg) of subboundary	$\gamma s (\pm .01)$	
	Dynamic	Equilibrium
0.65°	0.06	0.07
0.55°	0.16	0.19

These results indicate that the energy cusp, found under conditions of a moving grain boundary, is also present under equilibrium conditions. In a previous study of grain boundary energies in tin tricrystals (Aust and Chalmers 1950), the size of the dihedral angle opposite the grain boundary, whose orientation difference was varied from specimen to specimen, was studied as a function of annealing time at 220° C. In addition, the rate of movement of the triple point at the intersection of three grain boundaries was also determined. It was found that the angles between the grain boundaries reached equilibrium values well before the triple point reached its equilibrium position. This observation also indicates that grain boundary angles measured from grain boundaries which can move on further annealing may represent equilibrium values at the triple points.

The boundary energy cusp shown in Figs. 6 and 7 was predicted by Martius and Chalmers (1952), based on considerations of the free energy of a system which contains impurity atoms and a boundary. Their preliminary calculations for the possible dependence of relative boundary free energy upon difference in orientation showed a minimum in the energy at θ_{min} of about 0.5°; however, the exact calculated value of θ_{min} depends on the assumption of the magnitude of the volume strain field of the individual dislocations in a boundary. These calculations are based on a dislocation model using elasticity theory for the strain around the dislocation and the Seitz–Huntington model of the core distortion (Martius 1959). The calculated value of θ_{min} is consistent with the observed value of about 0.75° and suggests that the same phenomenon is

responsible in both cases. The energy cusp would be expected to be absent in the case of a pure metal with no impurity at the boundary. The present experimental data do indicate a decrease in the magnitude of the energy cusp with increasing purity of the aluminum, suggesting that the observed energy cusp may be related to impurity effects as considered by Martius and Chalmers (1952). Since impurities apparently exert a greater influence on the sub-boundary energies at the cusp position of $\theta \simeq 0.75°$, the energy at the latter value of θ should then be the one most sensitive to varying impurity content. This may account for the fact that the main difference in the curves of Figs. 6 and 7, for the 4-pass and 12-pass aluminum respectively, occurred at the cusp position. As was pointed out by Chalmers (1952), this cusp may be an important factor in the persistence of lineage substructure in metal crystals which are grown from the melt. The formation and/or retention of such boundaries in crystals would be energetically more favorable when impurities are present.

A recent study of absolute interfacial energies in copper having a purity of 99.98% showed no evidence of a cusp in the boundary energy versus orientation difference for lineage boundaries with misorientations (θ) from 0.65 to 3° (Gjostein and Rhines 1959). However, it is possible that a cusp, if present in copper, may have been missed since the θ values are given to $\pm 0.2°$, or that a cusp exists at a θ value below 0.65° in this relatively more impure material. One interesting consequence of the energy cusp found in aluminum is that a subboundary with a θ value of about 1.6° could form two subboundaries, each with a θ value of 0.8°, but with a *lower* total interfacial energy than the single, higher-angle subboundary. On an energetic basis, therefore, subboundaries with θ between 1.4 and 1.8° may then be absent; this was found to be the case in the present aluminum bicrystals (e.g. see Figs. 6 and 7).

The present energy cusp was not predicted by the theoretical treatment of Shockley and Read (1950) for dislocation boundaries, in which the effect of impurities was essentially neglected. The results of Figs. 6 and 7 are given in a single plot of relative boundary energy versus θ in Fig. 8; in addition, two curves are shown which were calculated from the Shockley and Read equation in the form of $\theta [A - \ln \theta]$, where $A = -0.5$ and $+0.5$. It should be noted that the exact position of the two calculated curves depends on the magnitude of θ at which the boundary energy is assumed to be unity. The latter θ value used here was 20° although this value has very little effect on the curves at small angles of θ.

The Shockley and Read curve with $A = +0.5$ is similar to that frequently observed in relative grain boundary energy experiments on impure materials. However, the curve with $A = -0.5$ describes the present data in the region of θ up to about 0.3° in which the boundary energy is least influenced by impurity due to the larger spacing of the dislocations in the boundary (Chalmers 1959). The curve with $A = -0.5$ might be expected, therefore, to represent better the simple dislocation model of the boundary, without impurities, than the curve with $A = +0.5$. In fact, a negative value for A of -0.3 may be obtained from the Shockley and Read calculations (Brooks 1952). In addition,
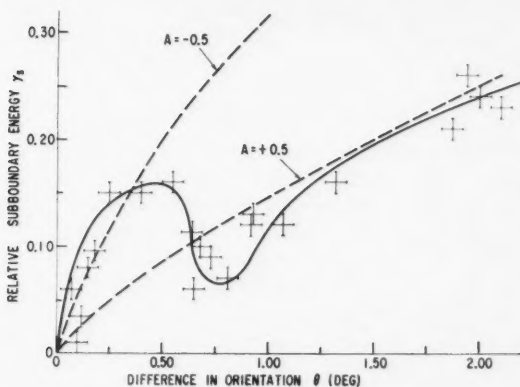
FIG. 8. Composite plot of relative energy versus θ data for the subboundaries in the 4-pass and 12-pass Al, together with theoretical $\theta\,(A - \ln\theta)$ curves (dashed) with $A = -0.5$ and $+0.5$.

the magnitude of the orientation difference, θ_{max}, where the relative boundary energy reaches a maximum, may be calculated from $\theta_{max} = e^{A-1}$. The θ_{max} values are then $13°$ and $35°$ for $A = -0.5$ and $+0.5$ respectively. The dislocation model of the boundary is probably a suitable description of the boundary structure for θ values approaching $13°$, but not for θ values as high as $35°$.

The above discussion of Fig. 8 indicates a possible explanation of the previous agreement of the experimental data on grain boundary energies with the Shockley and Read calculations far beyond the range of θ where the theory is no longer applicable. This explanation is based on the suggestion that the boundary energy of a "pure" metal may rise more rapidly with increasing θ than that of an "impure" metal. In the case of the usual relative boundary energy measurements on tricrystals, this argument assumes that the energy of the reference large-angle boundary is less influenced by impurity than that of the low- or medium-angle boundary whose relative energy is measured. This assumption appears to be reasonable since the energy of low-angle and medium-angle boundaries (i.e., $\theta \gtrsim 15°$) is markedly dependent on structure, while the energy of large-angle boundaries (i.e., $\theta \gtrsim 15°$) is independent of structure, except for twin boundaries and other possible special orientation relationships.

It is evident from the present experiments on subboundary energies, and from those on grain boundary migration (Rutter and Aust 1958, 1959), that the role of impurities on the properties of boundaries should not be neglected.

SUMMARY

The relative energy of subboundaries was studied as a function of orientation difference from 0.1 to $2°$ in aluminum bicrystals having two different effective impurity contents. A cusp was found in the energy versus θ relationship at $\theta \simeq 0.75°$, which is in agreement with the predictions of Martius and Chalmers

based on impurity effects at boundaries. The significance of the cusp with regard to substructures in metal crystals and previous work on boundary properties is discussed.

ACKNOWLEDGMENTS

REFERENCES

AUST, K. T.   1959.   To be published.
AUST, K. T. and CHALMERS, B.   1950.   Proc. Roy. Soc. A, **201**, 210.
AUST, K. T. and RUTTER, J. W.   1959.   Trans. Am. Inst. Met. Engrs. AIME **215**, 119.
BEAN, C. P., DeBLOIS, R. W., and NESBITT, L. B.   1959.   J. Appl. Phys. **30** (12), 1976.
BROOKS, H.   1952. *In* Metal interfaces (American Society for Metals, Cleveland), p. 20.
CHALMERS, B.   1959.   Private communication.
GJOSTEIN, N. A. and RHINES, F. N.   1959.   Acta Met. **7**, 319.
MARTIUS, U.   1959.   Private communication.
MARTIUS, U. and CHALMERS, B.   1952.   Discussion in imperfections in nearly perfect crystals (John Wiley & Sons), p. 371.
READ, W. T. and SHOCKLEY, W.   1950.   Phys. Rev. **78**, 275.
RUTTER, J. W. and AUST, K. T.   1958.   Acta Met. **6**, 375.

NEUTRON SOURCES FROM THE BERYLLIUM
REDUCTION OF PLUTONIUM DIOXIDE[1]

G. G. MICHAUD AND R. R. BOUCHER

ABSTRACT

Sintered neutron sources have been prepared by reacting plutonium dioxide with beryllium metal powder. The reaction, forming a plutonium–beryllium alloy, proceeded very slowly at 750° C but was nearly complete at 850° C. Sintered, non-friable agglomerates were obtained by heating the reacted mixtures at 1250 or 1450° C depending on the beryllium concentration. In the composition range of particular interest, i.e. Be/Pu atom ratios of 13:1 and above, the neutron output from the sintered products were from 93 to 98% of the theoretical neutron yield. The presence of BeO in the sinters was found to have negligible effect on the neutron output of the alloy. Studies of some factors affecting neutron output or sinter quality are also reported.

INTRODUCTION

Plutonium–beryllium alloy sources have been prepared in the past by two methods: by reducing plutonium fluoride with an excess of beryllium (Runnalls and Boucher 1956) and by heating the two metals together (Coffinberry and Tate 1958).

However, if the direct reduction of PuO_2 with Be could be used, a simpler, more economic method of preparation would result since there would be no need for fluorination or metal preparation.

According to published thermodynamic data (Coughlin 1954; Holley *et al.* 1958), BeO is more stable than PuO_2 at 1000° K since for the reaction

$$PuO_2 + 2Be \rightarrow Pu + 2BeO \tag{1}$$
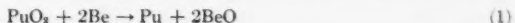
the free energy change $-\Delta F_{1000° \text{ K}} = 28 \pm 1$ kcal.

If excess Be is present, the equilibrium shifts further to the right because of alloy formation, and the reaction takes the form

$$PuO_2 + xBe \rightarrow PuBe_{13} + x - 15 \text{ Be} + 2BeO. \tag{2}$$
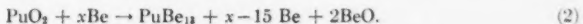
This paper describes procedures that have been developed for the preparation of neutron sources by this method. Also reported are:

(*a*) A brief study of the effect of temperature on the rate at which reaction (2) proceeds in vacuum.

(*b*) The effect of plutonium dispersal.

(*c*) The effect of compacting the reactants before sintering.

(*d*) The effect of partial melting of the alloy.

(*e*) The variation of the neutron yield of the sinters with composition.

EXPERIMENTAL PROCEDURE

(a) Materials

Plutonium dioxide of 99.9% purity was prepared by precipitating plutonium oxalate from a nitrate solution with oxalic acid crystals, then converting the oxalate to the dioxide by heating in air at 650° C for 3 hours. This material was found to correspond to the formula $PuO_{2.1}$ from the loss in weight after igniting a sample to constant weight at 1300° C (Drummond and Welsh 1957).

The isotopic composition of the plutonium as determined by mass spectrometer analysis was:

Pu^{239} 93.558±0.012 atom %,
Pu^{240} 5.948±0.010 atom %,
Pu^{241} 0.494±0.008 atom %.

Results obtained from a multichannel pulse analyzer showed that 2.6% of the total alphas were from Pu^{238} which corresponds to 0.011 atom % Pu^{238}. Hence, the calculated specific activity was 1.62×10^8 d.p.m. per mg Pu.

The plutonium dioxide and the 99.8% pure beryllium metal powder were both sized to −200 mesh.

(b) Preparation of the Samples

The powdered reagents were placed in a stoppered bottle and shaken by a mechanical vibrator. For early samples, the operation was carried out near a neutron counter to indicate the increase in neutron emission as mixing proceeded. The neutron output increased rapidly during the first minute but no observable increase resulted from mixing for longer periods. A mixing time of 2 minutes was considered adequate, therefore, for all subsequent samples.

The loose mixture was placed in a recrystallized-alumina crucible, 9/16 in. I.D.; it was then degassed by heating slowly under vacuum in a tungsten-element furnace to 400° C in 2 hours and was held at that temperature for 30 minutes. The furnace was then cooled and a cylindrical 30-g tantalum slug on a 1/2-in. diameter alumina disk was placed on top of the charge. Compression of the charge, which had to be avoided in degassing to prevent ejection of powder, was found necessary during sintering to obtain a uniform sinter from top to bottom.

Sintering was carried out by heating for 35 minutes in vacuum to either 1250° or 1450° C, depending on the beryllium concentration, and by holding the charge at this temperature for 10 minutes.

The choice of the sintering temperature was influenced by two considerations: the production of a satisfactory sinter and the prevention of partial liquation of the alloy.

A satisfactory sinter was defined as one that was dust-free, non-friable, and strong enough not to break in normal handling. According to the amount of excess Be that was used in reaction (2), the end products varied from highly ceramic to highly metallic. For samples with a high concentration of BeO in the end products (Be/Pu atom ratios around 15:1) a temperature from 1400 to 1450° C was found necessary to produce acceptable sinters. On the other hand, with highly metallic products (Be/Pu atom ratios 30:1 and upward), the desired sinter qualities could be obtained by heating at 1250° C.

It was also observed that samples with Be/Pu atom ratios above 30:1 could not be heated to 1450° C without causing partial liquation of the alloy accompanied by a decrease of 5 to 10% in the neutron output. This effect, discussed more fully later, was avoided by sintering samples in that range of compositions at 1250° C.

Since the evaporation loss of beryllium in vacuum was appreciable at 1450° C, the sintering time had to be kept short. If the sintering period was longer than 10 minutes, it was difficult to obtain a predictable Be/Pu atom ratio in the final product. All samples were, therefore, held for 10 minutes at the maximum temperature. The Be evaporation losses in this period were 5 to 8% at 1450° C, and less than 3% at 1250° C.

In establishing the Be/Pu atom ratio of the sintered samples, the Pu content was determined from the weight of oxide put in the charge. The Be content, which included Be as alloy and Be as BeO, was determined by subtracting the Be evaporation loss from the amount weighed for the charge.

(c) Neutron Counting Method

For neutron output measurement, the sintered sources were transferred from the glove-box into screw-top bottles. The neutron yields were determined in an area of low neutron background by direct comparison at room temperature of the neutron output of each source with that of a standard Pu-alpha-Be source using the simple paraffin-block counter described by Hanna and Runnalls (1956).

The standard Pu–Be source had been calibrated at the National Research Council, Ottawa (Geiger 1958), against the N.R.C. Ra-alpha-Be standard (N-200-1) which in turn had been compared with the N.B.S. primary standard. The neutron output of the Pu–Be standard was of the same order of magnitude as that of the sintered sources made in this work, i.e. $1.29 \pm 0.04 \times 10^5$ n/sec.

RESULTS

(a) Effect of Temperature on the Rate of Reduction of Plutonium Dioxide by Beryllium in Vacuum

It was determined from X-ray diffraction analysis that practically no reaction occurred between plutonium dioxide and excess beryllium after heating the reactants at 750° C for 30 minutes in vacuum. On the other hand, after the same time at 850° C, reduction of the PuO_2 was found to be well over 95% complete.

The X-ray diffraction patterns of residues from HCl leaches of sources sintered at 1250 or 1450° C showed only the lines of BeO, whereas the diffraction pattern of an unsintered sample containing 0.5 mol.% PuO_2 and 99.5 mol.% BeO showed all the lines of PuO_2 but one. This would indicate that in the sinters reduction had proceeded virtually to completion.

(b) The Effect of Plutonium Dispersal

With Pu–Be sources made by the conventional methods, the ideal distribution of the plutonium may be approached if the constituents are completely melted to a single liquid and cooled rapidly. In PuO_2–Be neutron sources, however, attempts to melt the alloy resulted in separation of Be-rich material from the sinter and in a decrease in the neutron yield.

The sintering operation itself gave only a limited increase in the neutron output, and it was therefore desirable to achieve mechanically a high degree of PuO_2 dispersal in the sample before sintering it. This could possibly best be done by reducing the maximum PuO_2 particle size.

Experiments were carried out to determine the effect of various mesh sizes of PuO_2 on the neutron yield after sintering. The samples, all with Be/Pu atom ratio of 100:1, were sintered at $1250°$ C according to the method described earlier. The neutron yields were determined after cooling with results as shown in Table I. The dusting loss during the sizing operation, the time taken to

TABLE I

Effect of PuO_2 mesh size on the neutron yield
after sintering at $1250°$ C for 10 minutes

PuO_2 mesh size	Neutron yield, % of theoretical
−100	87
−200	95
−300	96

produce −300-mesh PuO_2 were both appreciably higher than for −200-mesh material. Since only a slight improvement in the neutron yield resulted when using −300-mesh material, the results obtained with −200-mesh PuO_2 were considered satisfactory and this size was adopted for subsequent experiments.

Sintered samples from the PuO_2 sizing experiments were cross-sectioned and polished for microexamination. Because of the porosity in the samples, it was found preferable to examine them in the as-polished condition, without etching.

The effect of PuO_2 mesh size on the porosity of the samples sintered at $1250°$ C is shown at low magnification in Fig. 1A. The porosity, quite appreciable in the −100-mesh samples, decreased with decreasing coarseness of the PuO_2 particles and was relatively very low in the −300-mesh sample.

The effect of PuO_2 mesh size on the size of the larger $PuBe_{13}$ particles produced is shown at high magnification in Fig. 1B. The $PuBe_{13}$ phase appears as more or less circular islands of darker material in the bright beryllium matrix. The irregular black areas are pits caused partly by the porosity of the sample and partly by the removal of material in polishing. The diameter of the largest $PuBe_{13}$ particles observed was about 25 microns in the −100-mesh sample, 22 microns in the −200-mesh sample, and about 10 microns in the −300-mesh sample. There were very few large and intermediate size particles of $PuBe_{13}$; most were very fine.

(c) The Effect of Pressing the Mixed Reagents Before Sintering

The constituents for nine samples with Be/Pu atom ratios from 13:1 to 120:1 were mixed and then pressed at 20,000 p.s.i. The resulting green pellets

---

FIG. 1. As-polished sections of samples of 100:1 Be/Pu atom ratio sintered at $1250°$ C. PuO_2 mesh size is indicated in circles. Low magnification (A) shows the effect of PuO_2 mesh size on porosity. High magnification (B) shows the effect of PuO_2 mesh size on the size of the largest $PuBe_{13}$ particles produced. The light phase is Be matrix, the darker more or less circular phase is $PuBe_{13}$, and irregular black areas are voids.
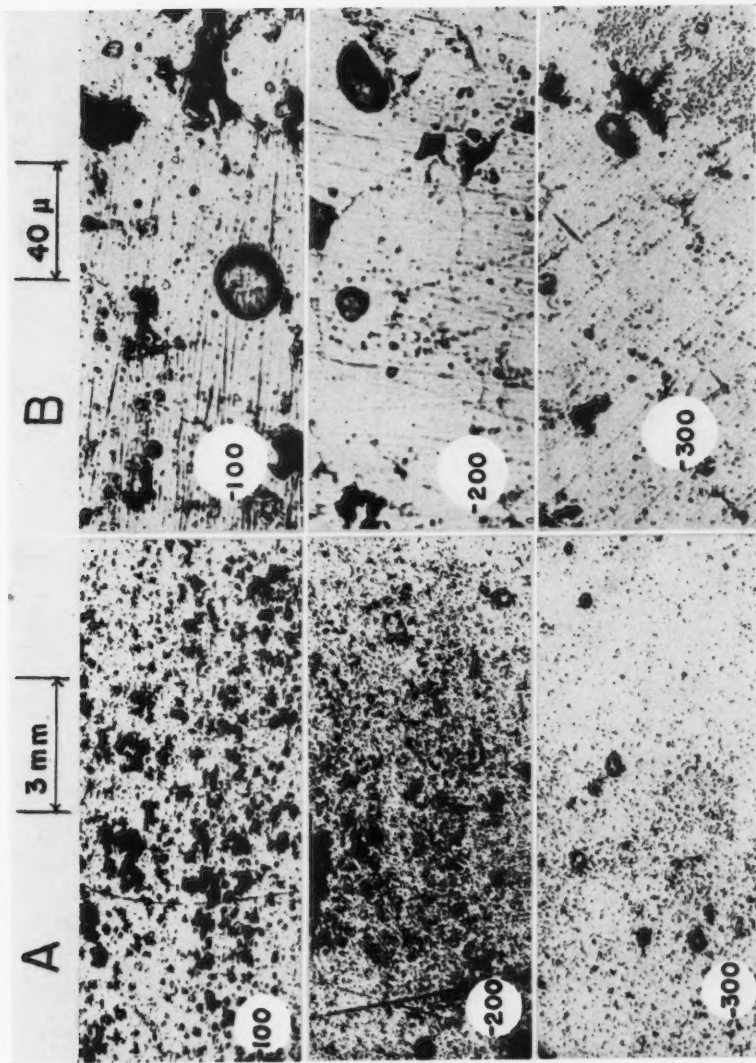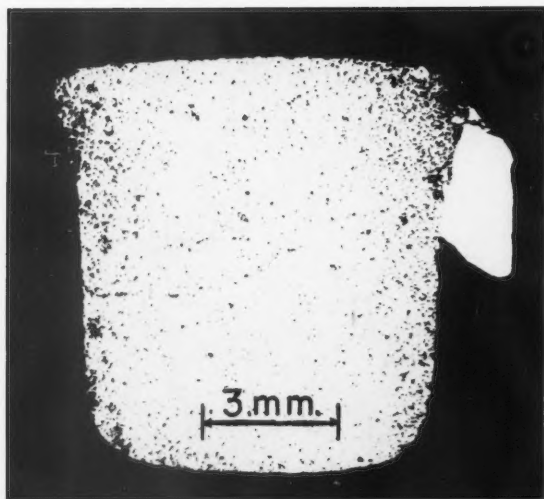
PLATE I

PLATE II

Fig. 2. As-polished section of a sample of 32:1 Be/Pu atom ratio in which partial liquation had started to occur while sintering at 1450° C. Melted material (top right) had exuded from the sinter.

were dust-free and could withstand normal handling without breaking or chipping. The pressed pellets could be heated in vacuum in 35 minutes to the sintering temperature without cracking or ejection of powder. Degassing, reduction, and sintering were, therefore, carried out in a continuous heating operation, eliminating the separate degassing step necessary in loose powder samples. The samples were held for 10 minutes at the sintering temperature, 1250 or 1450° C depending on the composition.

Pressed samples were sintered with and without the tantalum slug weight on top of the pellet. In both cases the pellets showed dimensional increases due to chemical reaction. In the presence of the slug pressure, the increase in height and diameter after sintering was less than 2%, while without the pressure, the dimensional increases varied from 2 to 6% with visible distortion of the cylindrical shape.

The neutron yields of the compacted samples after sintering were essentially the same as those from corresponding unpressed samples.

Compacted samples have also been sintered in tank argon following the same procedure with neutron yields generally 1 to 2% lower than those of equivalent sources sintered in vacuum.

(d) Effect of Partial Melting of the Alloy

No detectable amount of melting occurred when samples of Be/Pu with atom ratios between 7:1 and 30:1 were heated to 1450° C and held there for 10 minutes. However, if samples with ratios above 30:1 were heated to 1450° C, partial melting would occur and a drop of 3 to 10% in the neutron output would result. It appeared of interest to determine the reason for this drop in the neutron yield.

The polished cross section of a sample in which melting had just started to take place is shown at low magnification in Fig. 2. This sample had a Be/Pu atom ratio of 32:1 and had been sintered at 1450° C for 10 minutes. The bright Be-rich phase appearing at top right melted and separated from the sinter and had started to flow down into the space between the shrunken sinter and the crucible wall. This amount of alloy separation was enough to cause a drop of 4% in the neutron yield.

In order to study partial melting over the duration of the sintering operation, three samples with Be/Pu atom ratio of 100:1 were degassed, heated to 1350° C in 2 hours, and then cooled. The neutron output during heating and cooling was measured by a neutron counter positioned near the furnace. The neutron yields were later related to the absolute yields by a comparison of the cooled sample with a standard source. The time at which melting and freezing occurred was determined from the change of slope in the recorded output of a thermocouple placed near the sample.

In all three samples, two separate approximately equal decreases in the neutron output were observed. The first started when melting began at 1284° C and continued until 1350° C was reached where the power was reduced to allow cooling. The second decrease in the neutron yield started with the beginning of solidification at about 1284° C and continued until all the melted
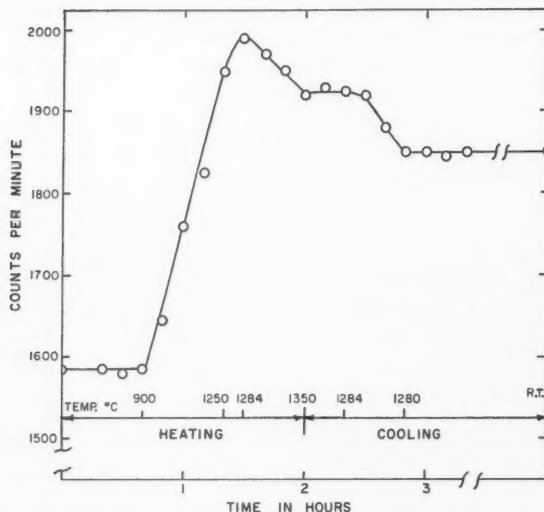
FIG. 3. Variation of the neutron emission rate from 100:1 Be/Pu atom ratio sample during heating to 1350° C and cooling to room temperature. Partial melting started at 1284° C.

material had solidified. The neutron output then remained constant to room temperature. The decrease in the neutron yield was approximately 4% during melting and the same during solidification. These observations are shown graphically in Fig. 3.

One of the samples was cross-sectioned and polished and is shown at low magnification in Fig. 4(a). An appreciable amount of material had melted and flowed out of the sinter to form a ring (torus) around the porous center portion. The two parts had about the same volume and analysis indicated Be/Pu atom ratios of 700:1 and 50:1 for the melted and unmelted parts respectively.

Thus, when partial melting occurs, it is a Be-rich phase that becomes liquid. The distribution of Pu is no longer uniform and this accounts for the first of the two observed drops in neutron yield.

The bottom left corner of the sample shown in Fig. 4(a) appears five times larger in Fig. 4(b). At this magnification considerable segregation of the acicular $PuBe_{13}$ phase can be observed in the area at left indicated by arrows. Higher magnification of a portion of this area of segregation (Fig. 4(c)) shows numerous $PuBe_{13}$ particles in the Be matrix and these have grown to considerable size. Growth of large $PuBe_{13}$ particles in the melted portion, probably resulting from slow cooling, could account for the drop in the neutron yield that occurred during solidification.

It was decided that samples with Be/Pu atom ratios greater than 30:1 would be sintered at 1250° C. This avoided melting, gave good sinters, and kept neutron output better than 94% of theoretical.
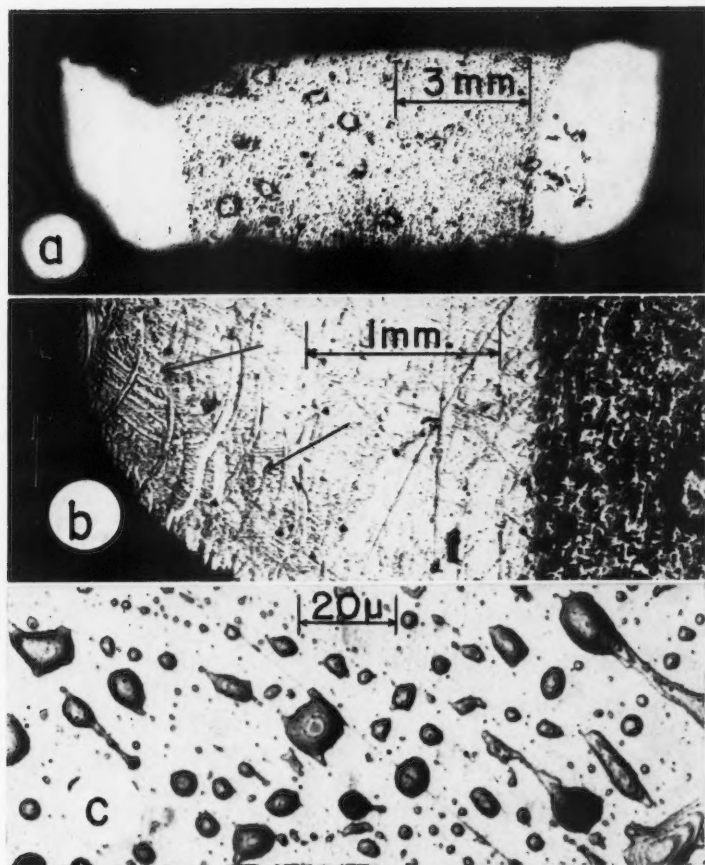
PLATE III

FIG. 4. As-polished section of a 100:1 Be/Pu atom ratio sample heated to 1350° C to produce partial melting.

(a) Low magnification shows a center portion that remained solid and two bright areas of Be-rich material which had melted and formed a ring around the sample.

(b) Shows the bottom left corner of sample in (a) at medium magnification where segregation of the $PuBe_{13}$ appears in the melted material (arrows).

(c) High magnification of the segregation area shows large particles of dark $PuBe_{13}$ in the light Be matrix.

(e) Variation of the Neutron Yield with Atom Ratio

The neutron yields from 22 sintered sources have been plotted in Fig. 5 to show the effect of the Be/Pu atom ratio on the observed yield of neutrons.
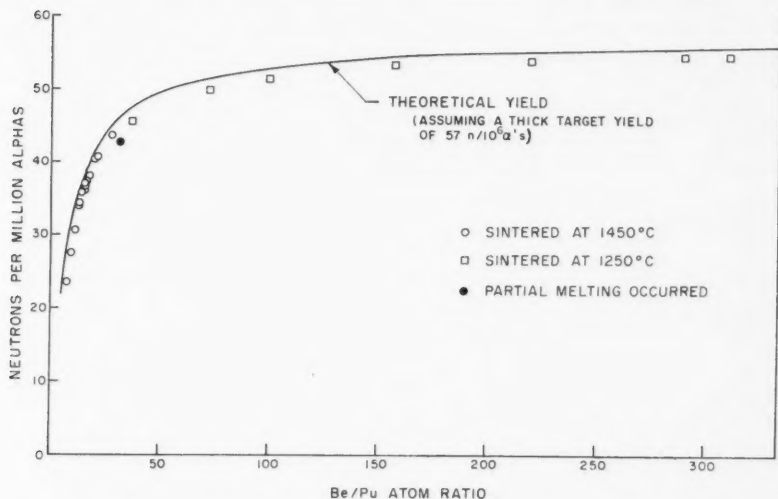

Fig. 5. The variation of the neutron yield with atom ratio for sintered sources made by the reduction of PuO_2 with Be.

The curve in Fig. 5 represents the theoretical neutron yield and was constructed from the expression used by Runnalls and Boucher (1956), i.e.

$$n_{max} = N \times S_{Be}/(N \times S_{Be} + S_{Pu})$$

where n/n_{max} = fraction of the maximum theoretical neutron yield,

N = Be/Pu atom ratio,
S_{Be} = Be atomic stopping power = 0.63,
S_{Pu} = Pu atomic stopping power = 4.6.

The value of the thick target yield, n_{max}, as determined by Runnalls and Boucher (1956) was 60 n/10⁶ alphas, when related to the Chalk River Ra-alpha-Be standard source. As mentioned by Hanna and Runnalls (1956), it appeared that the Chalk River standard, which had been calibrated against the Argonne National Laboratory source No. 38, was 5% too high with respect to the National Bureau of Standards Ra-gamma-Be source No. 2. Since it is now generally recognized that the N.B.S. standards are the more accurate, the quoted neutron output for the Chalk River standard has been lowered recently by 5%. Hence, the thick target neutron yield for Pu²³⁹ alphas on beryllium, n_{max}, has been decreased 5% to 57 n/10⁶ alphas.

It will be noted from Fig. 5 that good agreement is obtained between the highest observed values obtained in this work and the theoretical neutron

yields. The neutron yield obtained for a mixture produced according to the reaction

$$PuO_2 + 15Be \rightarrow PuBe_{13} + 2BeO$$

is 36.6 n/10^6 alphas which is in good agreement with the Runnalls and Boucher (1956) adjusted value of 36.7 n/10^6 alphas for $PuBe_{13}$. This would suggest that the BeO is not contributing significantly to the neutron output from the alloy.

Practical applications of neutron sources very often require minimum physical size for a given neutron yield. For a fixed amount of plutonium, sources with high Be/Pu atom ratios produce higher neutron yields than those with low ratios, but they also tend to become too bulky for many applications.

Konobeevsky (1955) reported that the maximum neutron yield per unit weight of alloy was obtained at a Be/Pu composition of 13:1, while results at Los Alamos indicated that higher yields per unit weight of alloy were obtainable at lower Be content than the $PuBe_{13}$ composition (Coffinberry and Waldron 1956). No report, however, has been found in the literature on the variation with composition of the neutron yield per unit volume of alloy. The maximum neutron yield per unit volume of alloy may be expected near the $PuBe_{13}$ composition provided the theoretical densities of the alloys are obtained. In order to approach theoretical density in the region of $PuBe_{13}$ composition, however, a temperature of 1600° C or more is required. The sinters in this work were heated to only 1450° C and it was to be expected, therefore, that the density of sinters near the $PuBe_{13}$ composition would be appreciably lower than the theoretical density.

It became desirable, therefore, to determine at what composition the maximum neutron yield per unit volume of sinter was obtained when sintering at 1450° C. The sinters were coated with wax and their volumes measured by a pycnometric method. The neutron yields in Fig. 5 were converted to neutrons per second per cubic centimeter of sinter and results were as shown in Table II.

TABLE II

Variation of the neutron yield per unit volume of products sintered at 1450° C for 10 minutes

Be/Pu atom ratio	Density, g/cm^3	Neutron yield, n/sec cm^3 of sinter
7.3	2.168	0.97 × 10^5
9.3	1.624	1.03
11.0	1.940	1.03
12.6	1.870	1.05
13.3	1.741	0.98
14.2	1.660	0.96
15.0	1.680	0.95
16.7	1.901	1.07
17.4	2.019	1.15
20.5	2.240	1.28
23.0	2.141	1.17
27.8	2.189	1.17
32.0	2.229	1.08

A maximum value is indicated at a Be/Pu atom ratio in the region of 20:1. Due to a marked difference in the sinterability of the various compositions at 1450° C, samples of 15:1 atom ratio reached only 40% of the theoretical density while samples of 20:1 ratio reached 60%.

DISCUSSION

From a series of more than 40 measurements of the yields of two standard sources, the possible errors in the comparative neutron yield measurements were estimated to be $\pm 2.5\%$. This is subject to a further deviation of $\pm 2.5\%$ to include the error of absolute standardization and intercalibration measurements of the primary standard.

The stability of Pu–Be neutron sources relies on the long half-life of Pu^{239} $(2.43 \times 10^4$ years). However, the isotopes Pu^{238}, Pu^{240}, and Pu^{241} are always present in varying amounts with Pu^{239} depending on the characteristics of the reactor and the length of time the plutonium was irradiated. Since the alpha half-lives of Pu^{238} and Pu^{240} are fairly long, 90 years and 6600 years respectively, the decrease in the neutron output from decay of these isotopes is slight; for the plutonium used in this work, it was calculated that the decrease in the alpha emission rate would be less than 0.5% in 20 years.

Pu^{241}, however, decays by beta-particle emission with a 12.9-year half-life to the alpha emitter Am^{241}, and if it is present in appreciable amounts, a gradual increase in the neutron output from Pu–Be sources will result. Since the plutonium used in this work was rather high in Pu^{241}, a growth correction factor was required and, as calculated by Hanna (1958), it amounted to 1.4% per year. The sources prepared by Be reduction of PuO_2 have been found satisfactory for many applications such as instrument calibration, or in low flux experimental work at A.E.C.L. In a special case, the need arose for a Pu–Be neutron source with a neutron output of the order of 10^7 n/sec, which would require about 100 g of plutonium. A Be/Pu atom ratio of about 18:1 was estimated for the completed source, which had a neutron output of 1.01×10^7 n/sec corresponding to 37.4 n/10^6 alphas or 92% of the theoretical neutron yield. These results confirmed the applicability of the small-scale work to the preparation of larger sources. A detailed account of the fabrication of this source has been published by Wauchope (1959).

CONCLUSIONS

Neutron sources can be prepared by reducing PuO_2 with Be and by sintering for 10 minutes at 1450 or 1250° C depending on the Be concentration.

A suitable size of PuO_2 particle for preparation of sources with high neutron yield was −200 mesh.

Pressing the reagents at 20,000 p.s.i. before sintering simplified the method by eliminating a separate degassing operation.

The sources, generally prepared under vacuum, have also been prepared in tank argon with neutron yields 1 to 2% lower than equivalent sources sintered in vacuum.

The optimum neutron yield per unit volume of sinter produced at 1450° C was obtained at a Be/Pu atom ratio in the region of 20:1.

CANADIAN JOURNAL OF PHYSICS. VOL. 38, 1960

REFERENCES

COFFINBERRY, A. S. and WALDRON, M. B. 1956. Progress in nuclear energy V, Metallurgy and Fuels, 397.
COUGHLIN, J. P. 1954. Contributions to data on theoretical metallurgy, U.S. Bureau Mines Bulletin 542.
DRUMMOND, J. L. and WELSH, G. A. 1957. J. Chem. Soc. 4781.
GEIGER, K. W. 1958. National Research Council Report APXNR-579.
HANNA, G. C. 1958. Private communication.
HANNA, G. C. and RUNNALLS, O. J. C. 1956. Can. J. Phys. **34,** 959.
HOLLEY, C. E., Jr., MULFORD, R. N. R., HUBER, E. J., Jr., HEAD, E. L., ELLINGER, F. H., and BJORKLUND, C. W. 1958. Second U. N. International Conference on the Peaceful Uses of Atomic Energy, paper P/701.
KONOBEEVSKY, S. T. 1955. Proceedings of the Academy of Science U.S.S.R. on the Peaceful Uses of Atomic Energy, 1–5 July, Chem. Science Vol. p. 362.
RUNNALLS, O. J. C. and BOUCHER, R. R. 1956. Can. J. Phys. **34,** 949.
TATE, R. E. and COFFINBERRY, A. S. 1958. Second U.N. International Conference on the Peaceful Uses of Atomic Energy, paper P/700.
WAUCHOPE, K. L. 1959. Journal of nuclear materials, **1** (2), 191.

NOTES

THE SOURCE OF NOISE IN EBULLIOMETRY

W. R. Blackmore

INTRODUCTION

As part of a study of ebulliometers (Blackmore 1959), it was necessary to determine whether the noise observed was produced by the ebulliometers themselves or by the temperature-sensing elements. Since these were two thermistors in a Wheatstone bridge circuit there was some suspicion that the observed noise might be thermistor "current noise" (Brophy 1954). To determine which source was responsible, first a dummy wire-wound bridge was tested at different amplifier gain settings and different bridge currents. Then the thermistor bridge was tested at the same bridge currents and amplifier gain settings with the thermistors instantaneously maintained at the same temperature in a special furnace. Finally the noise was measured with the thermistor bridge in the ebulliometers themselves and found to be significantly greater there.

APPARATUS

A d-c. Wheatstone bridge (Tinsley Co. Type 3352) was used in conjunction with a copper-block furnace (Blackmore, Part I, 1959) to calibrate the thermistors by measuring their resistances at different temperatures. The Wheatstone bridge unbalance voltages were detected with a Leeds–Northrup (Model 9835-B) d-c. microvolt amplifier and displayed on a Brown "Electronik" recorder (10 mv full scale). The temperature of the copper-block furnace was measured with a platinum resistance thermometer and a Mueller bridge.

After the thermistors (32A1 V.E. Co.) had been calibrated a matched pair was used in an a-c. bridge. The other two arms of the bridge were made of manganin wire of accurately known resistance, about equal to the resistance of the thermistors at the operating temperature, and were mounted in a thermally and electrically insulated can. The balancing decade boxes were Tinsley Co. (Type C-126) with 10×10, 1, 0.1, and 0.01 ohm steps. The boxes were oil-filled for temperature stability. A Tinsley Co. (Type C-133 A) decade box with steps of 10×0.001 and 0.0001 ohms was also used. All leads were shielded and all shields were connected to one ground point to avoid ground loops.

The circuit was arranged so that either the thermistor bridge or a wire-wound dummy bridge could be tested. The dummy bridge consisted of four manganin wire arms wound on a heavy brass former screwed into a heavy brass canister. This insured that all four arms were at the same temperature. The equivalent resistance of the bridge was about 150 ohms, which was the value expected for the thermistor resistances at the operating temperature.

The a-c. waveform for the bridge was produced by a double-pole double-throw chopper in series with a 2-volt lead–acid battery and a current-limiting resistor. The choppers were manufactured by the Tinsley Co. to the design of Dauphinee (1953). The bridge output was fed into a Liston–Becker Model 14 breaker amplifier (with its own choppers disconnected). This was done because no other a-c. amplifier was so conveniently available in the laboratory at that time. The amplifier output was then synchronously chopped and fed through a resistance–capacitance filter network to a Brown Electronik recorder. The choppers were operated at 8 cycles because the amplifier is designed to operate at this frequency.

RESULTS

The dummy-bridge sensitivity (Table I) in chart divisions per ohm change in the balancing arm is shown as a function of bridge current for different amplifier gain settings. The figures beside each entry in the table are measurements of the peak-to-peak noise at that setting.

TABLE I

Dummy-bridge sensitivity (div/Ω)

Amplifier gain setting	Bridge current		
	100 μa	250 μa	500 μa
14-1	1,150±0	2,900±1/4	5,800±1/4
16-1	2,950±0	7,400±1/4	14,800±1/4
18-1	8,000±1/2	20,000±1/2	40,000±1/2
20-1	24,500±1	56,000±2	112,000±2

To test the thermistor bridge both thermistors were frozen into a solder plug (50:50 lead:tin, m.p. 225° C) side by side along with a platinum resistance thermometer. This plug was then submerged in oil in the copper-block furnace and maintained at temperatures comparable to the operating temperatures to be expected in the usual ebulliometer. Once again the noise was measured at different amplifier gain settings and different bridge currents. It will be observed (Table II) that this noise was slightly larger than it had been with the dummy bridge. This extra noise is probably "thermistor current noise" (Brophy 1954). If it were extra pickup then the noise at lower currents and amplifier gains should have been greater for the thermistor bridge than the dummy bridge. Or if because of their position in the furnace the thermistors were more exposed to hum pickup then turning the heater power off in the furnace would have changed the noise in the trace. This did not happen.

TABLE II

Thermistor bridge sensitivity (div/Ω)

Amplifier gain setting	Bridge current		
	100 μa	250 μa	500 μa
14-1	1,200±0	3,100±1/4	6,200±1/4
16-1	3,100±0	8,000±1/2	16,000±1/2
18-1	8,500±1/2	21,500±1	42,500±2
20-1	25,000±2	60,000±2 1/2	110,000±3

To convert the noise measurement for the thermistor bridge to an equivalent temperature fluctuation is quite simple. We will treat the noise of $\pm 1/2$ division at gain 16-1 and 250-μa bridge current as though it were all produced by a temperature fluctuation in only one thermistor in the bridge. At 8000 divisions per ohm (from Table II) a change of $\pm 1/2$ division represents a peak-to-peak noise of ± 62.5 $\mu\Omega$ (micro-ohms). Now from the thermistor calibration it is known that this has a temperature coefficient of about $4\,\Omega/^\circ$ C at 100° C. Therefore the noise of ± 62.5 $\mu\Omega$ is equivalent to ± 15 μ° C peak-to-peak. But we know (Blackmore 1959, ref. 4) that even for pure solvent in a typical ebulliometer the noise level is about ± 150 μ° C. It is reasonable to conclude therefore that the noise is truly produced by the ebulliometer and not by the electrical equipment or the thermistors.

ACKNOWLEDGMENT

The author wishes to thank H. H. Wood for his valuable advice and help during the course of this work.

BLACKMORE, W. R. 1959. Can. J. Chem. **37**, 1508.
——— 1959. Can. J. Chem. **37**, 1517.
——— 1959. Can. J. Phys. **37**, 1365.
——— 1960. Rev. Sci. Instr. March.
BROPHY, J. J. 1954. J. Appl. Phys. **25**, 222.
DAUPHINEE, T. M. 1953. Can. J. Phys. **31**, 577.
VICTORY ENGINEERING Co., Springfield Road, Union, N.J.

SOME SENSITIVITIES OF ION GAUGES

WM. McGOWAN AND LARKIN KERWIN

Schulz (1957) has published some characteristics of the Bayard–Alpert ionization gauge used at pressures above 10^{-5} mm Hg. In this pressure region, it has been the practice to use ionization gauges such as the RCA 1949. It has become known that many triodes are suitable for such measurements. In particular, the 826-A twin-filament triode which is currently available on the surplus market at about one dollar has been used in several laboratories.

PROCEDURE

Two 826-A triodes, a Bayard–Alpert type gauge (Veeco RG-75), and a standard Macleod gauge were exposed to the same atmospheres of various gases. As recommended by Schulz, the tubes were operated at 100 μa of electron current instead of the usual 10 ma in order to permit the application of high pressure.

With the plates (ion collectors) of the tubes kept at ground potential, the filaments were biased at $+22.5$ volts and the grids at $+150$ volts. Pressures

were varied from 10^{-5} to 10^{-2} mm Hg. Ion currents of from 10^{-8} to 10^{-5} amp were measured with a G-R model 1230-A electrometer.

The following considerations are discussed at length by Schulz (1957). For a given gas and a given electron current, the number of ions formed varies as the pressure. The variation is essentially a linear one up to about 0.1 mm Hg. This has been verified in the case of the 826-A's to 0.01 mm Hg. For a given pressure, the ion current varies linearly with the electron current up to saturation. For a given pressure and electron current, different gases will give rise to different ion currents. The ratio of such ion currents for two gases should be the same as the ratio of their cross sections for ion formation when bombarded by electrons of a known energy. We shall refer to the latter as a "reference ratio" although it is a measured one. Such cross sections are given by Massey and Burhop (1952). The electron energy involved varies in our case from 127.5 ev to about the ionization potential, depending on where between the grid and collector the ions are formed. For some gases the ratio of cross sections is moderately constant over much of this range.

From these considerations, the ion current is seen to be proportional to the electron current and to the pressure. The sensitivity S of the gauge may then be defined from the relation

$$i_+ = i_- pS$$

where S may be given in units of (mm Hg)$^{-1}$. For comparison purposes, argon may be used as a standard, when the ratio S_x/S_A (of the sensitivity for the gas x to that for argon) may be compared with the reference ratio (X_x/X_A) where X is the cross section for ion formation.

RESULTS

TABLE I

Observed and calculated sensitivities and ratios

| Gas | Ref. cross section (Massey 1952) (100 ev) | Sensitivity (mm Hg)$^{-1}$ | | | Ratio S_x/S_A | | | |
| | | Schulz, B-A* | This note | | Ref. ratio | Schulz, B-A | This note | |
			Veeco	826-A			Veeco	826-A
Argon	3.5×10^{-16} cm^2	18	3.5	2.6	—	—	—	—
Helium	0.35	2.5	0.5$_8$	0.3$_5$	0.10	0.14	0.16	0.13
N$_2$	2.87	12.0	2.8	2.0	0.82	0.67	0.80	0.75
O$_2$	2.89	—	3.5	2.5	0.82	—	1.0	0.94
Air	2.87 (assumed)	—	3.3	2.1$_5$	0.82	—	0.94	0.81

*B-A: Bayard-Alpert.

In this work, we have used the value 3.5×10^{-16} cm^2 for the apparent cross section for ion formation in argon. Schulz appears to have used the value 2.64 corresponding to singly charged ions. The value 3.5 brings all of Schulz's published ratios into better agreement with the reference ratios except for He. A high value for helium is also evident in our work. There is little doubt that this is due to the presence of impurities, a very small amount of which would have considerable effect in the case of helium. The other measured ratios are

in good agreement with the reference ratios when the experimental errors both in this work and in that used to obtain the values of the cross sections are taken into account.

The sensitivity of the Veeco gauge published here is much lower than the official value (10 for N_2). In fact, it was found that two series of sensitivities could be found for this gauge when used at high pressures. The sets of values were consistent with cross sections, and the tube could be "switched" from high to low ion current by positioning a magnet near the tube, and by other means which appeared to us to suggest two stable configurations of space charge in the tube. This effect has been noted elsewhere (Carmichael, private communication; Carter 1959, and references cited therein) and has been claimed to be due rather to the charging of the glass envelope to either filament or plate potential. We have reported here the low values which were the more stable in the range of pressures used by us. The 826-A tube did not display this dual sensitivity.

CARMICHAEL, J. H. Vacuum-Electronic Engineering Co. Private communication.
CARTER, G.   1959.   Nature, **183**, 1619.
MASSEY, H. S. W. and BURHOP, E. H. S.   1952.   Electronic and ionic impact phenomena (The Clarendon Press, Oxford).
SCHULZ, G. J.   1957.   J. Appl. Phys. **28**, 1149.

THE STATUS OF THE CANADIAN NEUTRON STANDARD*

K. W. GEIGER

The neutron emission rate of the radium beryllium (α,n) source No. N-200-1 of the National Research Council has recently been measured absolutely by two methods (Geiger and Whyte 1959; Geiger 1959). The source was prepared in 1948 and contained 183 mg of radium element in the form of the carbonate, mixed with 2000 mg of beryllium powder and pressed into a pellet to ensure physical stability. The pellet is contained in a cylindrical Monel capsule of 2-mm wall thickness, both the diameter and the height being 19 mm.

The first method of calibration, based on slowing down and capturing of the neutrons in a manganese bath resulted in an emission rate of $(3.22_0 \pm 0.05) \times 10^6$ neutrons sec^{-1} as of July 1958. For the second method an auxiliary polonium fluorine (α,n) source was used and by following the growth of the radioactive

reaction product, sodium-22, the neutron emission rate could be established. This source was then compared, in a manganese sulphate bath, with the radium beryllium (α,n) source with a resulting emission rate of $(3.16\pm0.10)\times10^6$ sec^{-1} as of the same date. Since the spectra of a radium beryllium (α,n) source and of a polonium fluorine (α,n) source are very different (Szilvasi *et al.* 1960) a somewhat larger error had to be assigned to this value because of uncertainties in the intercomparison. The weighted mean of both results is:

$$Q = (3.20_8\pm0.05)\times10^6 \text{ neutrons per second as of July 1958.}$$

Calibrations carried out at different laboratories might be expected to give somewhat different values for the neutron emission rate and comparisons between various laboratories are therefore desirable. This is facilitated by the fact that relative intercomparisons of sources can be carried out with greater accuracy than an absolute calibration. Therefore, it is only necessary to compare the absolute standards of the laboratories concerned. Probably the first results of such intercomparisons (in 1951 and 1954) have been published by Hughes (1954). Whereas the maximum spread of calibrations was 20% in 1951 it was reduced to 10% in 1954, showing that definite improvements in neutron source calibrations were made. The most recent set of intercomparisons was carried out by Larsson (1958), who had compared the Swedish standard with standards from U.S.S.R., Belgium, Switzerland, U.S.A., and United Kingdom. The maximum spread between calibrations found was 4%.

During the first half of 1959 the Canadian neutron standard was compared with standards of various laboratories. The prime requirement when such measurements are carried out is to make sure that the emission rate of the Canadian standard did not change during the course of these intercomparisons, possibly caused by rough handling in shipment. Measurements carried out at this laboratory after completion of the intercomparisons indicated that no change in neutron emission rate occurred within the precision of the measurement of $\pm0.3\%$.
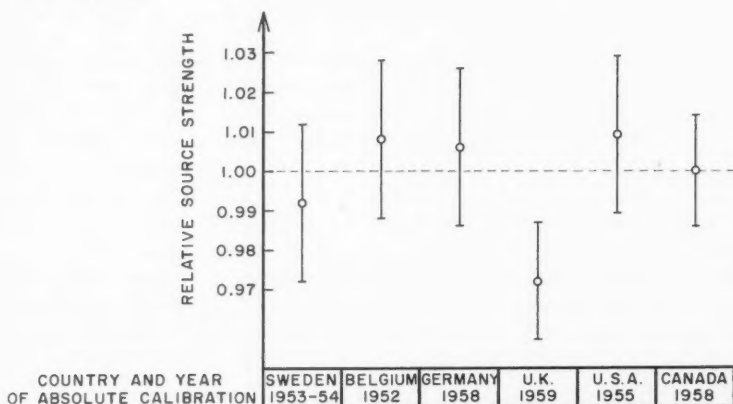

FIG. 1. Relative source strengths of neutron standards of various laboratories in relation to the Canadian standard (arbitrarily set equal to 1.000).

The results of the intercomparisons are shown in Table I and Fig. 1. Column 1 of this table gives the laboratory where a standard was calibrated absolutely and with which the Canadian standard was compared.

TABLE I

Absolute neutron standard and year of calibration	Date and place of inter-comparison with N.R.C. standard	Measured ratio, $Q_x/Q_{N.R.C.}$	Absolute source strength at date of intercomparison		$Q_{N.R.C.}$ on (x)scale, n/sec × 10^{-6}	Ratio of (x)scale to N.R.C. scale (relative source strength)
			Q_x, n/sec × 10^{-6}	$Q_{N.R.C.}$, n/sec × 10^{-6}		
(1)	(2)	(3)	(4)	(5)	(6)	(7)
Sweden AB Atomenergi 1953–1954	Stockholm Jan. 1959	0.843 ±0.8%	2.68$_7$ ±2%	3.21$_4$	3.18$_7$	0.992
Belgium Union Minière du Haut Katanga 1952	Brussels Feb. 1959	2.485 ±0.12%	8.05$_7$ ±2%	3.21$_8$	3.24$_2$	1.008
Germany Physikalisch Technische Bundesanstalt 1958	Braunschweig Mar. 1959	.6038 ±0.3%	1.95$_4$ ±2%	3.21$_6$	3.23$_4$	1.006
U. K. National Physical Laboratory	Teddington June 1959	—	—	3.21$_9$	3.12$_5$ ±1.5%	0.972
U. S. A. National Bureau of Standards 1955	Ottawa July 1959	0.3654 ±1%	1.187 ±2%	3.22$_0$	3.24$_8$	1.009
Canada National Research Council 1958	—	—	3.20$_9$ ±1.5%	3.20$_9$ (July)	—	1.000

Column 2 shows where the intercomparisons were carried out and column 3 shows the ratio found. All except the U.S. source were radium beryllium (α,n) sources which have similar neutron spectra. This allows intercomparisons to be made without great difficulties. The U.S. source is a radium beryllium (γ,n) source with consequently a much less energetic neutron spectrum. The comparison was carried out using manganese sulphate bath activation and the same corrections for fast neutron losses from the (α,n) source were applied as described in a previous paper (Geiger and Whyte 1959).

Column 4 shows the values obtained for the absolute calibrations, corrected for the date of intercomparison. The Swedish source was calibrated by Larsson (1954, 1955) using four different methods: by associated particle counting from the $T^3(d,n)He^4$ reaction, by absolute counting with a proton recoil chamber, and by neutron density measurements in aqueous solutions with small BF_3 chambers and gold foils. The Belgian source was calibrated by De Troyer and Tavernier (1954) by a neutron density measurement in water with gold foils. The emission rate of the German source was determined by Kolb and von Droste (1959) using the same method. Since a British standard was not

available at the time, Axton (1959) calibrated the Canadian source directly by activation of a manganese sulphate bath. The U.S. source N.B.S. I was also calibrated by the bath method and, in addition, by a neutron density measurement in water using foils (De Juren *et al.* 1955a, b). N.B.S. II was very carefully compared with N.B.S. I (Mosburg 1959).

Column 5 gives the neutron emission rate of the Canadian standard corrected for the increase in neutron emission due to growth of polonium-210 within the source and column 6 shows its emission rate as found by comparison with the other standards.

The last column shows the relative neutron emission rates for the Canadian standard (relative source strength) as obtained by the various laboratories; the Canadian value has arbitrarily been set equal to 1.000. Figure 1 shows this in graphical form with only the errors in the absolute calibration given.

The agreement between the calibrations is satisfactory, the maximum spread being 3.7%. Although, considering this relatively small spread, the errors quoted by the various authors appear to be rather large it has to be kept in mind that in calibrating of neutron sources certain corrections are applied which are identical in some of the calibration methods. An error in this correction will therefore produce a systematic shift of all such calibrations. This applies in particular to the correction for fast neutron capture in oxygen in the case of bath methods. Any further improvements in the standardization of neutron sources depends mainly on the better knowledge of such correction factors.

AXTON, E. J. 1959. Unpublished.
DE JUREN, J. A., PADGETT, D. W., and CURTISS, L. F. 1955a. J. Research Natl. Bur. Standards, **55**, 63.
DE JUREN, J. A. and CHIN, J. 1955b. J. Research Natl. Bur. Standards, **55**, 311.
DE TROYER, A. and TAVERNIER, G. C. 1954. Acad. roy. Belg., Bull. classe Sci., **40**, 150.
GEIGER, K. W. 1959. Can. J. Phys. **37**, 550.
GEIGER, K. W. and WHYTE, G. N. 1959. Can. J. Phys. **37**, 256.
HUGHES, D. J. 1954. Nucleonics, **12** (12), 26.
KOLB, M. and VON DROSTE, G. 1959. Unpublished.
LARSSON, K.-E. 1954. Arkiv Fysik, **7**, 323.
———— 1955. Arkiv Fysik, **9**, 293.
———— 1958. J. Nuclear Energy, **6**, 322.
MOSBURG, E. R., Jr. 1959. J. Research Natl. Bur. Standards, **62**, 189.
SZILVASI, A., GEIGER, K. W., and DIXON, W. R. 1960. J. Nuclear Energy. Part A (Reactor in science). In press.

HIGH-ENERGY GAMMA RADIATION FROM Ag^{110m}

H. W. Taylor and S. A. Scott

Following a recent coincidence study of 253-day Ag^{110m} (Taylor and Scott 1959) a search was made for a weak high-energy gamma-ray component observed by der Mateosian and Goldhaber (1950), Wilson (1950), and Dzhelepov and Iaritsyma (1956) using photodisintegration techniques. The energy of the radiation as determined by these workers was found to be between 1.66 and 2.2 Mev. An intensity of 3×10^{-4} photons per disintegration was quoted by Wilson, and 8×10^{-4} photons per disintegration by Dzhelepov and Iaritsyma.

The observation of gamma radiation from Ag^{110m} with a scintillation counter in this energy region is complicated by the presence of prominent sum lines in the gamma-ray pulse height spectrum at 1596, 1825, 2041, 2166, and 2270 kev (Taylor and Scott 1959). Since the single counting rate is proportional to the solid angle ω, and the sum coincidence rate to ω^2, the present investigation was carried out with a relatively small solid angle. The detector consisted of a $1\frac{1}{2}$ in. diam.$\times1$ in. long NaI (Tl) crystal mounted on a Du Mont 6292 photomultiplier tube. It was mounted vertically in a lead castle with walls 3 in. thick and an open top. The source, 0.4 mc of Ag^{110m} formed by a slow-neutron irradiation of spec. pure silver, was placed 175 cm vertically above the crystal. The pulses from the counter were amplified with a linear amplifier (resolving time 1 μsec) and analyzed with a Baird-Atomic 20-channel pulse height analyzer.

The pulse height distribution (corrected for background pulses) in the range 1300 to 1800 kev is shown in Fig. 1. The shapes of the photopeaks (dashed lines) at 1510 and 1560 kev were calculated using the gamma-ray intensities of Dzhelepov (1957, 1958). The shapes of the sum lines at 1596 and 1825 kev were calculated from geometrical considerations and the known intensities of the contributing low-energy gamma-rays (656, 885, and 940 kev). Compton distributions have been excluded for the sake of simplicity since they do not affect the shape of the spectrum substantially at 1700 kev. The solid curve in the figure represents the sum of the photopeaks and sum lines mentioned above. It is in good agreement with the experimental points only if one includes an additional peak at 1730 ± 30 kev, as shown. (Of course, the spectrum obtained using photopeaks and sum lines only will not exhibit the smearing due to Compton distributions; this is evident from the figure.) The gamma ray associated with this feature, assuming it is not spurious, has an intensity of $(6\pm2)\times10^{-4}$ photons per disintegration, a value which agrees with the observations of Wilson, and Dzhelepov and Iaritsyma.

About one half-life after the first experimental runs, this region of the spectrum was re-examined with the same geometry, etc. The counting rates at the maxima of the 1385- and 1510-kev photopeaks were reduced to $50\pm2\%$ of their original values, as expected. The corresponding reduction for the
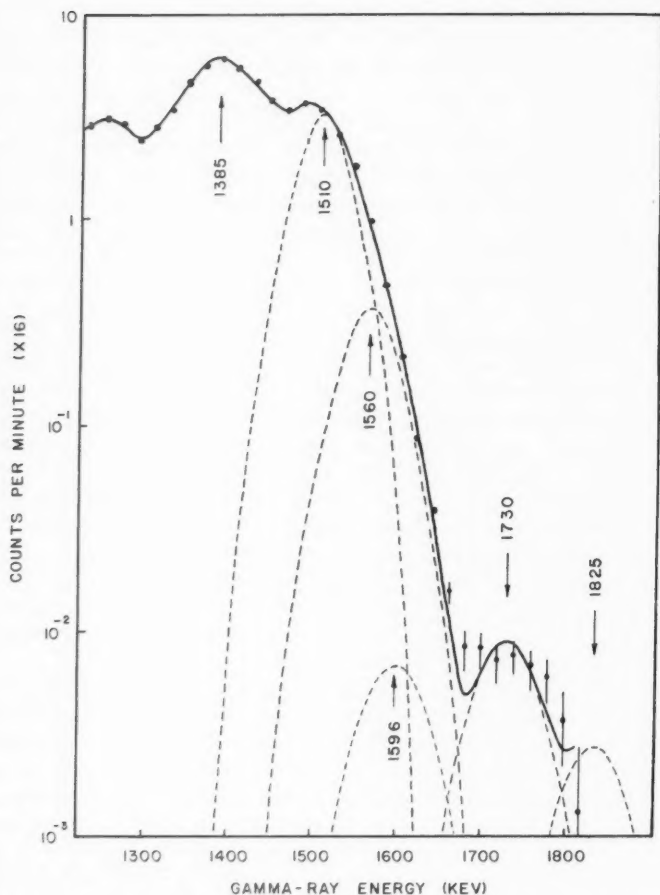
Fig. 1. Pulse height spectrum between 1300 and 1800 kev obtained with a 1½ in. × 1 in. NaI (Tl) crystal. Source-to-crystal distance, 175 cm.

1730-kev peak was 70±30%, the large error being due solely to the low counting rate. It seems improbable that the peak at 1730 kev is due to an accidental summing of pulses in the amplifier since this would result in a reduction factor of 25%. The only accidental sum peaks expected in this region of the spectrum have energies of 1700 (940+760) and 1755 (940+815) kev. Their intensities have been estimated as less than 10% of the 1730-kev peak. On the other hand, the only genuine sum lines in this region are those at 1596 and 1825 kev with intensities as shown in Fig. 1. Thus it would appear that the peak at 1730 kev is not due to either genuine or accidental superposition of pulses due to the strong gamma rays present. Furthermore, it seems unlikely to be due to a contaminant in view of the high purity of the silver used.

The peak at 1730 kev does not correspond to the crossover transition of energy 1.8 Mev mentioned in Nuclear Data Cards. Furthermore, this feature cannot be the Compton maximum for a gamma ray of this energy. Taking the inflection point at 1770 kev gives a gamma-ray energy of about 2 Mev. To check on this possibility, however, the region above 1800 kev was examined with the spectrometer. Although the counting rate was found to be slightly in excess of the background, no structure was observed in the pulse height spectrum which had an intensity appropriate to a 1730-kev Compton maximum. The counting rates encountered were comparable to that at 1800 kev and are probably due to weak genuine sum lines with energies in excess of 1825 kev (Taylor and Scott 1959).

The observations reported here suggest that the observed peak is due to a single gamma ray of energy 1730 ± 30 kev emitted by Ag^{110m}. Since its energy lies in the range 1.6 to 2.2 Mev, and no gamma ray of comparable intensity is observed at 1825 kev, it is probably the same radiation reported by other workers.

A transition of this energy cannot be included in the Cd^{110} level scheme at the present time. It is of interest to note, however, that other weak gamma rays of energies 575, 541, 499, 471, and 437 kev have been reported by Cork *et al.* (1950), none of which have been incorporated into the level scheme. Two of these gamma-ray energies, when added to 1730 kev, give sum energies worthy of note: $1730+541 = 2271$ kev and $1730+437 = 2167$ kev. Sum lines of these energies previously reported by the authors are known to arise from genuine coincidences between intense gamma rays: $656+1510 = 2166$ kev, $885+1385 = 760+1510 = 2270$ kev. If the 1730- and 437-kev gamma rays form a cascade, there must be a level in Cd^{110} at 1730 kev (see Taylor and Scott (1959) for level scheme). Similarly, a cascade containing the 1730- and 541-kev gamma radiations implies a level at 2395 kev. (The alternative, a level at 1197 kev, would conflict with the systematic trends of the energy levels of even–even nuclei.) The inclusion of other weak gamma rays into the decay scheme is not facilitated by either possibility, however, and the clarification of the situation must await further work with the weak gamma radiations.

Cork, J. M., Rutledge, W. C., Branyan, C. E., Stoddard, A. E., Childs, W. J., and LeBlanc, J. M. 1950. Phys. Rev. **80**, 286.
Dzhelepov, B. S. and Iaritsyma, I. A. 1956. Izvestia Akad. Nauk. S.S.S.R. Ser. Fiz. **20**, 343.
Dzhelepov, B. S. and Zhukovsky, N. N. 1958. Nuclear Physics, **6**, 655.
Dzhelepov, B. S., Zhukovsky, N. N., and Kondakov, N. G. 1957. Izvestia Akad. Nauk. S.S.S.R. Ser. Fiz. **21**, 973.
der Mateosian, E. and Goldhaber, M. 1950. Phys. Rev. **78**, 326.
Taylor, H. W. and Scott, S. A. 1959. Phys. Rev. **114**, 121.
Wilson, R. 1950. Phys. Rev. **79**, 1004.

LETTERS TO THE EDITOR

Under this heading brief reports of important discoveries in physics may be published. These reports should not exceed 600 words and, for any issue, should be submitted not later than six weeks previous to the first day of the month of issue. No proof will be sent to the authors.

Frequency Measurement of Standard Frequency Transmissions[1,2]

Measurements are made at Ottawa, Canada, using N.R.C. caesium-beam frequency resonator as reference standard (with an assumed frequency of 9 192 631 770 c.p.s.). Frequency deviations from nominal are quoted in parts per 10^{10}. A negative sign indicates that the frequency is below nominal.

Date, January 1960	MSF, 60 kc/s	GBR, 16 kc/s		KK2XEI, 60 kc/s
		8½-hour average*	24-hour average	
1	−167	−171	−169	N.M.
2	−173	−170	−170	N.M.
3	−170	−171	−169	N.M.
4	−173	−168	−169	−83
5	−169	−168	−167	−82
6	−173	−170	−170	−84
7	−167	−172	−171	−85
8	−175	−168	−170	−85
9	−173	−170	−172	N.M.
10	−173	−170	−170	N.M.
11	−167	−169	−169	−84
12	−165	−171	−171	−87
13	−172	−170	−169	−85
14	−166	−170	−172	−85
15	−176	−172	−170	−85
16	−179	−170	−170	N.M.
17	−168	−173	−172	N.M.
18	−188	−171	−170	−87
19	N.M.	−172	−170	−83
20	N.M.	−167	−168	−84
21	N.M.	−175	−172	−88
22	N.M.	−170	−171	N.M.
23	−176	−174	−175	N.M.
24	−177	−178	−176	N.M.
25	−173	−178	−176	N.M.
26	−175	−173	−174	N.M.
27	−176	−175	−175	N.M.
28	−180	−177	−174	−89
29	−179	−174	−174	−89
30	−178	−175	−175	N.M.
31	−182	−177	−177	N.M.
Midmonthly mean	−174	−172	−172	−85
Midmonthly mean of WWV	−159			

NOTE: N.M. no measurement.

*Time of observations: 00.00 to 07.00 and 22.30 to 24.00 U.T.

S. N. KALRA

[1] Issued as N.R.C. No. 5628.
[2] Cf. Kalra, S. N. 1959. Can. J. Phys. 37, 1328.

NOTES TO CONTRIBUTORS

Canadian Journal of Physics

MANUSCRIPTS

General.—Manuscripts, in English or French, should be typewritten, double spaced, on paper $8\frac{1}{2} \times 11$ in. **The original and one copy are to be submitted.** Tables and captions for the figures should be placed at the end of the manuscript. Every sheet of the manuscript should be numbered. Style, arrangement, spelling, and abbreviations should conform to the usage of recent numbers of this journal. Greek letters or unusual signs should be written plainly or explained by marginal notes. Characters to be set in boldface type should be indicated by a wavy line below each character. Superscripts and subscripts must be legible and carefully placed. Manuscripts and illustrations should be carefully checked before they are submitted. Authors will be charged for unnecessary deviations from the usual format and for changes made in the proof that are considered excessive or unnecessary.

Abstract.—An abstract of not more than about 200 words, indicating the scope of the work and the principal findings, is required, except in Notes.

References.—References should be listed **alphabetically by authors' names,** unnumbered, and typed after the text. The form of the citations should be that used in current issues of this journal; in references to papers in periodicals, titles should not be given and only initial page numbers are required. The names of periodicals should be abbreviated in the form given in the most recent *List of Periodicals Abstracted by Chemical Abstracts.* All citations should be checked with the original articles and each one referred to in the text by the authors' names and the year.

Tables.—Tables should be numbered in roman numerals and each table referred to in the text. Titles should always be given but should be brief; column headings should be brief and descriptive matter in the tables confined to a minimum. Vertical rules should not be used. Numerous small tables should be avoided.

ILLUSTRATIONS

General.—All figures (including each figure of the plates) should be numbered consecutively from 1 up, in arabic numerals, and each figure referred to in the text. The author's name, title of the paper, and figure number should be written in the lower left corner of the sheets on which the illustrations appear. Captions should not be written on the illustrations.

Line drawings.—Drawings should be carefully made with India ink on white drawing paper, blue tracing linen, or co-ordinate paper ruled in blue only; any co-ordinate lines that are to appear in the reproduction should be ruled in black ink. Paper ruled in green, yellow, or red should not be used. All lines must be of sufficient thickness to reproduce well. Decimal points, periods, and stippled dots must be solid black circles large enough to be reduced if necessary. Letters and numerals should be neatly made, preferably with a stencil (**do NOT use typewriting**) and be of such size that the smallest lettering will be not less than 1 mm high when the figure is reduced to a suitable size. Many drawings are made too large; originals should not be more than 2 or 3 times the size of the desired reproduction. Whenever possible two or more drawings should be grouped to reduce the number of cuts required. In such groups of drawings, or in large drawings, full use of the space available should be made; the ratio of height to width should conform to that of a journal page ($4\frac{3}{4} \times 7\frac{1}{2}$ in.), but allowance must be made for the captions. **The original drawings and one set of clear copies (e.g. small photographs) are to be submitted.**

Photographs.—Prints should be made on glossy paper, with strong contrasts. They should be trimmed so that essential features only are shown and mounted carefully, with rubber cement, on white cardboard, with no space between those arranged in groups. In mounting, full use of the space available should be made. **Photographs are to be submitted in duplicate;** if they are to be reproduced in groups one set should be mounted, the duplicate set unmounted.

REPRINTS

A total of 100 reprints of each paper, without covers, are supplied free. Additional reprints, with or without covers, may be purchased at the time of publication.

Charges for reprints are based on the number of printed pages, which may be calculated approximately by multiplying by 0.6 the number of manuscript pages (double-spaced typewritten sheets, $8\frac{1}{2} \times 11$ in.) and including the space occupied by illustrations. Prices and instructions for ordering reprints are sent out with the galley proof.

Contents